JHEP

Published for SISSA by Springer

Received: December 19, 2020
Revised: January 15, 2021
Accepted: February 9, 2021
Published: April 7, 2021

Nucleon momentum fraction, helicity and transversity from 2+1-flavor lattice QCD

Nucleon Matrix Elements (NME) collaboration

Santanu Mondal,[a] **Rajan Gupta,**[a] **Sungwoo Park,**[a,b] **Boram Yoon,**[c] **Tanmoy Bhattacharya,**[a] **Bálint Joó**[d] **and Frank Winter**[e]

[a] *Los Alamos National Laboratory, Theoretical Division T-2, Los Alamos, NM 87545, U.S.A.*

[b] *Center for Nonlinear Studies, Los Alamos National Laboratory, Los Alamos, New Mexico 87545, U.S.A.*

[c] *Los Alamos National Laboratory, Computer Computational and Statistical Sciences, CCS-7, Los Alamos, NM 87545, U.S.A.*

[d] *Oak Ridge Leadership Computing Facility, Oak Ridge National Laboratory, Oak Ridge, TN 37831, U.S.A.*

[e] *Jefferson Lab, 12000 Jefferson Avenue, Newport News, Virginia 23606, U.S.A.*

E-mail: santanu@lanl.gov, rajan@lanl.gov, sungwoo@lanl.gov, boram@lanl.gov, tanmoy@lanl.gov, joob@ornl.gov, fwinter@jlab.org

Abstract: A detailed analysis of the systematic uncertainties in the calculation of the isovector momentum fraction, $\langle x \rangle_{u-d}$, helicity moment, $\langle x \rangle_{\Delta u - \Delta d}$, and the transversity moment, $\langle x \rangle_{\delta u - \delta d}$, of the nucleon is presented using high-statistics data on seven ensembles of gauge configurations generated by the JLab/W&M/LANL/MIT collaborations using 2+1-flavors of dynamical Wilson-clover quarks. The much higher statistics have facilitated better control over all systematics compared to previous lattice calculations. The least understood systematic — excited-state contamination — is quantified by studying the variation of the results as a function of different estimates of the mass gap of the first excited state, obtained from two- and three-point correlation functions, and as a function of the pion mass M_π. The final results are obtained using a simultaneous fit in the lattice spacing a, pion mass M_π and the finite volume parameter $M_\pi L$ keeping leading order

https://doi.org/10.1007/JHEP04(2021)044

JHEP04(2021)044

corrections. The data show no significant dependence on the lattice spacing and some evidence for finite-volume corrections. Our final results, in the $\overline{\text{MS}}$ scheme at 2 GeV, are $\langle x \rangle_{u-d} = 0.155(17)(20)$, $\langle x \rangle_{\Delta u - \Delta d} = 0.183(14)(20)$ and $\langle x \rangle_{\delta u - \delta d} = 0.220(18)(20)$, where the first error is the overall analysis uncertainty assuming excited-state contributions have been removed, and the second is an additional systematic uncertainty due to possible residual excited-state contributions. These results are consistent with phenomenological global fit values.

Keywords: Lattice QCD, Lattice Quantum Field Theory

ArXiv ePrint: 2011.12787

JHEP04(2021)044

Contents

1 Introduction 1

2 Lattice methodology 2

3 Moments and matrix elements 4

4 Correlation functions and moments 5

5 Controlling excited state contamination 6

6 Chiral, continuum and infinite volume extrapolation 13

7 Conclusions 15

A Plots of the ratio $C^{\mathrm{3pt}}_{\mathcal{O}}(\tau;t)/C^{\mathrm{2pt}}(\tau)$ 18

B Results of excited-state fits 25

C Renormalization of the operators 29

1 Introduction

Steady progress in both experiment and theory is providing an increasingly detailed description of the hadron structure in terms of quarks and gluons. The distributions of quarks and gluons within nucleons are being probed in experiments at the Relativistic Heavy Ion Collider (RHIC) at BNL [1, 2], Jefferson Lab [3] and the Large Hadron Collider at CERN. Experiments at the planned electron-ion collider [4] will significantly extend the range of Bjorken x and the momentum transfer Q^2, and further improve our understanding. From these data, and using higher order calculations of electroweak and strong corrections, the phenomenological analyses of experimental data (global fits) are providing parton distribution functions (PDFs) [5, 6], transverse momentum dependent PDFs (TMDs) [7], and generalized parton distributions (GPDs) [8]. These distributions are not measured directly in experiments [9, 10], necessitating phenomenological analyses that have involved different theoretical inputs.

Lattice QCD calculations are beginning to provide such input, and a review of the cross-fertilization between the two efforts has been presented in refs. [11, 12]. With increasing computing power and advances in algorithms, the precision of lattice QCD calculations has increased significantly and there now exist many quantities for which there is good agreement with experimental results, and for some, the lattice results are the most precise as reviewed in the recent Flavor Lattice Averaging Group (FLAG) 2019 report [13].

JHEP04(2021)044

Overall, the calculations of the isovector momentum fraction, and the helicity and transversity moments are now reaching precision comparable to that for nucleon charges, which are the zeroth moments of the distributions and obtained from the matrix elements of local quark bilinear operators [13, 14]. In this work, high-statistics lattice data allowed us to make five significant improvements over results presented in ref. [16]. These improvements are summarized in the concluding section 7.

Calculations for the three first moments, $\langle x \rangle_{u-d}$, $\langle x \rangle_{\Delta u - \Delta d}$ and $\langle x \rangle_{\delta u - \delta d}$, have been done on seven ensembles generated using 2+1-flavors of Wilson-clover quarks by the JLab/W&M/LANL/MIT collaborations [15]. The high-statistics data at three values of lattice spacings a, two values of the pion mass, $M_\pi \approx 170$ and $\approx 270\,\text{MeV}$, and on a range of large volumes, characterized by $M_\pi L$, allow us to carry out a simultaneous fit in these three variables to address the associated systematic uncertainties. In the analysis of the two- and three-point correlation functions from each ensemble, we present a careful investigation of the dependence of the results on the spectra of possible, *a priori* unresolved, excited states included in the fits to remove excited-state contamination (ESC). Concretely, the full analysis is carried out using three strategies to estimate the mass gap of the first excited state from the two- and three-point correlation functions, and we use the spread in the results to assign a second systematic uncertainty to account for possible remaining contributions from excited-states.

Our final results, given in eq. (6.2), are $\langle x \rangle_{u-d} = 0.155(17)(20)$, $\langle x \rangle_{\Delta u - \Delta d} = 0.183(14)(20)$ and $\langle x \rangle_{\delta u - \delta d} = 0.220(18)(20)$ in the $\overline{\text{MS}}$ scheme at 2 GeV. These estimates are in good agreement with other lattice and phenomenological global fit results as discussed in section 6. The most extensive and precise results from global fits are for the unpolarized moments of the nucleons, the momentum fraction $\langle x \rangle_q$, while those for the helicity fraction, the polarized moment $\langle x \rangle_{\Delta q}$, have a large spread and our lattice results are consistent with the smaller error global fit values at the lower end. Lattice QCD results for the transversity $\langle x \rangle_{\delta q}$ are a prediction due to lack of sufficient experimental data [11, 12].

The paper is organized as follows: in section 2, we briefly summarize the lattice parameters and methodology. The definitions of moments and operators investigated are given in section 3. The two- and three-point functions calculated, and their connection to the moments, are specified in section 4. The analysis of excited state contributions and the extraction of the ground state matrix elements is presented in section 5. Results for the moments after the chiral-continuum-finite-volume (CCFV) extrapolation are given in section 6, and compared with other lattice calculations and global fit values. We end with conclusions in section 7. The data and fits used to remove excited-state contamination are shown in appendix A, results of excited-state fits in appendix B, and the calculation of the renormalization factors, $Z_{VD,AD,TD}$, for the three operators and values of the renormalized moments in appendix C.

2 Lattice methodology

This work follows closely the methodology described in ref. [16], with two major differences. The first improvement is the calculation here uses 2+1-flavors of Wilson-clover fermions

JHEP04(2021)044

Ensemble ID	a (fm)	M_π (MeV)	$L^3 \times T$	$M_\pi L$	τ/a	$N_{\rm conf}$	$N_{\rm HP}$	$N_{\rm LP}$
$a127m285$	0.127(2)	285(3)	$32^3 \times 96$	5.85	$\{8, 10, 12, 14\}$	2001	8,004	256,128
$a094m270$	0.094(1)	270(3)	$32^3 \times 64$	4.11	$\{10, 12, 14, 16\}$	1464	4,392	140,544
$a094m270L$	0.094(1)	269(3)	$48^3 \times 128$	6.16	$\{8, 10, 12, 14, 16, 18\}$	4501	18,004	576,128
$a091m170$	0.091(1)	169(2)	$48^3 \times 96$	3.75	$\{8, 10, 12, 14, 16\}$	4015	16,060	513,920
$a091m170L$	0.091(1)	169(2)	$64^3 \times 128$	5.08	$\{8, 10, 12, 14, 16\}$	1533	7,665	245,280
$a073m270$	0.0728(8)	272(3)	$48^3 \times 128$	4.82	$\{11, 13, 15, 17, 19\}$	4477	17,908	573,056
$a071m170$	0.0707(8)	167(2)	$72^3 \times 192$	4.26	$\{13, 15, 17, 19, 21\}$	2100	12,600	201,600

Table 1. Lattice parameters of the 2+1-flavor clover ensembles generated by the JLab/W&M/LANL/MIT collaborations and analyzed in this study. We give the lattice spacing a, pion mass M_π, lattice size $L^3 \times T$, the values of source-sink separation τ simulated, the number of configurations analyzed, and the total number of high precision (HP) and low precision (LP) measurements made. The values of τ in red are used in the fits to remove ESC.

in a clover-on-clover unitary formulation of lattice QCD, whereas the clover-on-HISQ formulation was used in ref. [16]. The clover action includes one iteration of stout smearing with weight $\rho = 0.125$ for the staples [17]. The tadpole corrected tree-level Sheikholeslami-Wohlert coefficient $c_{SW} = 1/u_0$ [18], where u_0 is the fourth root of the plaquette expectation value, is very close to the nonperturbative value determined, a posteriori, using the Schrödinger functional method [19], a consequence of the stout smearing. The update of configurations was carried out using the rational hybrid Monte Carlo (RHMC) algorithm [20] as described in ref. [21].

Parameters of the seven clover ensembles generated by the JLab/W&M/LANL/MIT collaborations [15] and used in the analysis are summarized in table 1. The range of lattice spacings covered is $0.071 \le a \le 0.127$ fm and of lattice size is $3.7 \le M_\pi L \le 6.2$. So far simulations have been carried out at two pion masses, $M_\pi \approx 270$ and 170 MeV. These seven data points allow us to perform chiral-continuum-finite-volume fits to obtain physical results.

The second improvement is higher statistics data that has allowed a more robust analysis of three strategies for evaluating ESC. Table 1 also gives the number of configurations, the source-sink separations τ, high precision (HP) and low precision (LP) measurements made to cost-effectively increase statistics using the bias-corrected truncated-solver method [22, 23].

The parameters used to construct the Gaussian smeared sources [14, 16, 24, 25] are given in table 2. To construct the smeared source, the gauge links were first smoothened using twenty hits of the stout algorithm with $\rho = 0.08$ and only the spatial staples were included [17]. The root-mean-square size of the Gaussian smearing, $\sqrt{\int dr\, r^4 S^\dagger S / \int dr\, r^2 S^\dagger S}$ with $S(r)$ the value of the smeared source at radial distance r, was adjusted to be between 0.71–0.76 fm to reduce ESC. The quark propagators from these smeared sources were generated by inverting the Dirac operator (same as what was used to generate the lattices) using the multigrid algorithm [26–28]. These propagators were then used to construct the two- and three-point correlation functions.

JHEP04(2021)044

Ensemble ID	m_l	$c_{\rm SW}$	Smearing Parameters $\{\sigma, N_{\rm KG}\}$	RMS smearing radius
$a127m285$	-0.2850	1.2493	{5, 50}	5.79(1)
$a094m270$	-0.2390	1.2054	{7, 91}	7.72(3)
$a094m270L$	-0.2390	1.2054	{7, 91}	7.76(4)
$a091m170$	-0.2416	1.2054	{7, 91}	7.64(3)
$a091m170L$	-0.2416	1.2054	{7, 91}	7.76(4)
$a073m270$	-0.2070	1.1701	{9, 150}	9.84(1)
$a071m170$	-0.2091	1.1701	{10, 185}	10.71(2)

Table 2. The parameters used in the calculation of the clover propagators. The hopping parameter for the light quarks, κ_l, in the clover action is given by $2\kappa_l = 1/(m_l + 4)$. $c_{\rm SW}$ is the Sheikholeslami-Wohlert improvement coefficient in the clover action. The parameters used to construct Gaussian smeared sources [29], $\{\sigma, N_{\rm KG}\}$ in the Chroma convention [30], are given in the fourth column where $N_{\rm KG}$ is the number of applications of the Klein-Gordon operator and σ controls the width of the smearing. The resulting root-mean-square radius of the smearing in lattice units, defined as $\sqrt{\int dr\, r^4 S^\dagger S / \int dr\, r^2 S^\dagger S}$ with $S(r)$ the value of the smeared source at radial distance r, is given in the last column.

3 Moments and matrix elements

The first moments of spin independent (or unpolarized), $q = q_\uparrow + q_\downarrow$, helicity (or polarized), $\Delta q = q_\uparrow - q_\downarrow$, and transversity, $\delta q = q_\top + q_\perp$ distributions, are defined as

$$\langle x \rangle_q = \int_0^1 x\, [q(x) + \overline{q}(x)]\, dx\,, \tag{3.1}$$

$$\langle x \rangle_{\Delta q} = \int_0^1 x\, [\Delta q(x) + \Delta\overline{q}(x)]\, dx\,, \tag{3.2}$$

$$\langle x \rangle_{\delta q} = \int_0^1 x\, [\delta q(x) + \delta\overline{q}(x)]\, dx\,, \tag{3.3}$$

where $q_{\uparrow(\downarrow)}$ corresponds to quarks with helicity aligned (anti-aligned) with that of a longitudinally polarized target, and $q_{\top(\perp)}$ corresponds to quarks with spin aligned (anti-aligned) with that of a transversely polarized target.

These moments, at leading twist, are extracted from the forward matrix elements of one-derivative vector, axial-vector and tensor operators within ground state nucleons at rest. The complete set of the relevant twist two operators are

$$\begin{aligned} \mathcal{O}^{\mu\nu}_{V^a} &= \overline{q}\gamma^{\{\mu}\overleftrightarrow{D}^{\nu\}}\tau^a q\,, \\ \mathcal{O}^{\mu\nu}_{A^a} &= \overline{q}\gamma^{\{\mu}\overleftrightarrow{D}^{\nu\}}\gamma^5\tau^a q\,, \\ \mathcal{O}^{\mu\nu\rho}_{T^a} &= \overline{q}\sigma^{[\mu\{\nu]}\overleftrightarrow{D}^{\rho\}}\tau^a q\,, \end{aligned} \tag{3.4}$$

where $q = \{u, d\}$ is the isodoublet of light quarks and $\sigma^{\mu\nu} = (\gamma^\mu\gamma^\nu - \gamma^\nu\gamma^\mu)/2$. The derivative $\overleftrightarrow{D}^\nu \equiv \frac{1}{2}(\overrightarrow{D}^\nu - \overleftarrow{D}^\nu)$ consists of four terms defined in ref. [16]. Lorentz indices within { } in eq. (3.4) are symmetrized and within [] are antisymmetrized. It is also

JHEP04(2021)044

implicit that, where relevant, the traceless part of the above operators is taken. Their renormalization is carried out nonperturbatively in the regularization independent RI′-MOM scheme as discussed in appendix C. A more detailed discussion of these twist-2 operators and their renormalization can be found in refs. [31] and [32].

In our setup to calculate the isovector moments, we work with $\tau^a = \tau^3$ and fix the spin of the nucleon state to be in the "3" direction. With these choices, the explicit operators calculated are

$$\mathcal{O}^{44}_{V^3} = \overline{q}\left(\gamma^4 \overleftrightarrow{D}^4 - \frac{1}{3}\boldsymbol{\gamma}\cdot\overleftrightarrow{\mathbf{D}}\right)\tau^3 q\,, \tag{3.5}$$

$$\mathcal{O}^{34}_{A^3} = \overline{q}\gamma^{\{3}\overleftrightarrow{D}^{4\}}\gamma^5\tau^3 q\,, \tag{3.6}$$

$$\mathcal{O}^{124}_{T^3} = \overline{q}\sigma^{[1\{2]}\overleftrightarrow{D}^{4\}}\tau^3 q\,. \tag{3.7}$$

The forward matrix elements (ME) of these operators within the ground state of the nucleon with mass M_N are related to the moments as follows:

$$\langle 0|\mathcal{O}^{44}_{V^3}|0\rangle = -M_N\,\langle x\rangle_{u-d}\,, \tag{3.8}$$

$$\langle 0|\mathcal{O}^{34}_{A^3}|0\rangle = -\frac{iM_N}{2}\,\langle x\rangle_{\Delta u-\Delta d}\,, \tag{3.9}$$

$$\langle 0|\mathcal{O}^{124}_{T^3}|0\rangle = -\frac{iM_N}{2}\,\langle x\rangle_{\delta u-\delta d}\,. \tag{3.10}$$

The moments are, by construction, dimensionless.

4 Correlation functions and moments

To construct the two- and three-point correlation functions needed to calculate the matrix elements, the interpolating operator $\mathcal{N}$ used to create/annihilate the nucleon state is

$$\mathcal{N} = \epsilon^{abc}\left[q_1^{aT}(x)C\gamma^5\frac{(1\pm\gamma_4)}{2}q_2^b(x)\right]q_1^c(x)\,, \tag{4.1}$$

where $\{a,b,c\}$ are color indices, $q_1, q_2 \in \{u,d\}$ and $C = \gamma_4\gamma_2$ is the charge conjugation matrix in our convention. The nonrelativistic projection $(1\pm\gamma_4)/2$ is inserted to improve the signal, with the plus and minus signs applied to the forward and backward propagation in Euclidean time, respectively [31]. At zero momentum, this operator couples only to the spin-$\frac{1}{2}$ states. The zero momentum two-point and three-point nucleon correlation functions are defined as

$$\mathbf{C}^{\text{2pt}}_{\alpha\beta}(\tau) = \sum_{\boldsymbol{x}}\langle 0|\mathcal{N}_\alpha(\tau,\boldsymbol{x})\overline{\mathcal{N}}_\beta(0,\mathbf{0})|0\rangle \tag{4.2}$$

$$\mathbf{C}^{\text{3pt}}_{\mathcal{O},\alpha\beta}(\tau,t) = \sum_{\boldsymbol{x}',\boldsymbol{x}}\langle 0|\mathcal{N}_\alpha(\tau,\boldsymbol{x})\mathcal{O}(t,\boldsymbol{x}')\overline{\mathcal{N}}_\beta(0,\mathbf{0})|0\rangle \tag{4.3}$$

where α, β are spin indices. The source is placed at time slice 0, the sink is at τ and the one-derivative operators, defined in section 3, are inserted at time slice t. Data have been

JHEP04(2021)044

Ensemble ID	$aM_N^{\{4\}}$	$aM_N^{\{4^{N\pi}\}}$	$a\Delta M_1^{\{2\}}$	$a\Delta M_1^{\{4\}}$	$a\Delta M_1^{\{4^{N\pi}\}}$	$a\Delta M_1^{\{2^{\text{free}}\}}$ $\langle x\rangle_{u-d}$	$a\Delta M_1^{\{2^{\text{free}}\}}$ $\langle x\rangle_{\Delta u-\Delta d}$	$a\Delta M_1^{\{2^{\text{free}}\}}$ $\langle x\rangle_{\delta u-\delta d}$
$a127m285$	0.6181(19)	0.6167(14)	0.413(46)	0.376(52)	0.326(20)	0.359(35)	0.706(58)	0.64(11)
$a094m270$	0.4709(35)	0.4706(25)	0.349(91)	0.273(63)	0.2643(95)	0.521(64)	0.647(66)	0.510(66)
$a094m270L$	0.4668(12)	0.4656(9)	0.357(19)	0.303(42)	0.249(27)	0.344(26)	0.400(53)	0.466(29)
$a091m170$	0.4163(23)	0.4119(19)	0.346(22)	0.293(45)	0.195(19)	0.311(48)	0.441(64)	0.424(61)
$a091m170L$	0.4143(25)	0.4093(28)	0.307(25)	0.252(36)	0.157(11)	0.297(43)	0.388(52)	0.34(11)
$a073m270$	0.3719(11)	0.3716(8)	0.321(18)	0.229(41)	0.217(24)	0.311(16)	0.457(14)	0.431(16)
$a071m170$	0.3286(19)	0.3257(16)	0.275(21)	0.216(36)	0.151(12)	0.352(56)	0.545(23)	0.498(32)

Table 3. Results for the nucleon mass $aM_N^{\{4\}}$ and $aM_N^{\{4^{N\pi}\}}$ obtained from the two four-state fits to the two-point functions. The next six columns give the values of the mass gap, $a\Delta M_1 \equiv a(M_1 - M_0)$, of the first excited state obtained from different fits studied in this work. The notation used is $\{2\}$ ($\{4\}$) is a two-state (four-state) fit to the two-point functions, $\{4^{N\pi}\}$ is a four-state fit to the two-point functions with a prior with a narrow width for $a\Delta M_1$ corresponding to the non-interacting $N\pi$ state. In the three $\{2^{\text{free}}\}$ cases, the $a\Delta M_1$ are determined from fits to the three-point functions used to extract the three moments as explained in the text.

accumulated for the values of τ specified in table 1, and for each τ for all intermediate times $0 < t < \tau$.

To isolate the various contributions, projected 2- and 3-point functions are constructed as

$$C^{2\text{pt}} = \text{Tr}(\mathcal{P}_{2\text{pt}}\mathbf{C}^{2\text{pt}}) \tag{4.4}$$

$$C^{3\text{pt}}_{\mathcal{O}} = \text{Tr}(\mathcal{P}_{3\text{pt}}\mathbf{C}^{3\text{pt}}_{\mathcal{O}})\,. \tag{4.5}$$

The projector $\mathcal{P}_{2\text{pt}} = \frac{1}{2}(1+\gamma_4)$ in the nucleon correlator gives the positive parity contribution for the nucleon propagating in the forward direction. For the connected 3-point functions, $\mathcal{P}_{3\text{pt}} = \frac{1}{2}(1+\gamma_4)(1+i\gamma^5\gamma^3)$ is used. With these spin projections, the three moments are obtained using eqs. (3.8), (3.9) and (3.10).

To display the data, we construct the ratios

$$R_{\mathcal{O}}(\tau;t) = C^{3\text{pt}}_{\mathcal{O}}(\tau;t)/C^{2\text{pt}}(\tau) \tag{4.6}$$

that give the ground state matrix element in the limits $t \to \infty$ and $(\tau - t) \to \infty$. These ratios are shown in figures 5–10 in appendix A. We re-emphasize that this ratio is not used to extract the ground state matrix element $\langle 0|\mathcal{O}|0\rangle$ used in the analysis, which is instead obtained from fits to $C^{3\text{pt}}_{\mathcal{O}}(\tau;t)$ with input of spectral quantities from $C^{2\text{pt}}(\tau)$. These fits are carried out within a single-elimination jackknife process, which is used to get both the central values and the errors.

5 Controlling excited state contamination

A major challenge to precision results is removing the contribution of excited states in the three-point functions. These occur because the lattice nucleon interpolating operator $\mathcal{N}$,

JHEP04(2021)044

defined in eq. (4.1), couples to the nucleon, all its excitations and multiparticle states with the same quantum numbers. Previous lattice calculations have shown that these ESC can be large [16, 33–35]. The strategy to remove these artifacts in this work is the same as described in ref. [16]: reduce ESC by using smeared sources in the generation of quark propagators and then fit the data at multiple source-sink separations τ using the spectral decomposition of the correlation functions (eqs. (5.1) and (5.2)) keeping as many excited states as possible without overparameterizing the fits. In this work, we examine three strategies, $\{4, 3^*\}$, $\{4^{N\pi}, 3^*\}$ and $\{4, 2^{\text{free}}\}$, that use different estimates of the excited state masses in the fits as described below.

The spectral decomposition of the zero-momentum two-point function, $C_{2\text{pt}}$, truncated at four states, is given by

$$C_{2\text{pt}}(\tau) = \sum_{i=0}^{3} |\mathcal{A}_i|^2 e^{-M_i \tau} \,. \tag{5.1}$$

We fit the data over the largest time range, $\{\tau_{\text{min}} - \tau_{\text{max}}\}$, allowed by statistics, i.e., by the stability of the covariance matrix, to extract the M_i and $\mathcal{A}_i$, the masses and the amplitudes for the creation/annihilation of the four states by the interpolating operator $\mathcal{N}$. We perform two types of four-state fits. In the fit denoted $\{4\}$, we use the empirical Bayesian technique described in the ref. [21] to stabilize the three excited-state parameters. In the second fit, denoted $\{4^{N\pi}\}$, we use a normally distributed prior for M_1, centered at the lower of the non-interacting energy of $N(-\mathbf{1})\pi(\mathbf{1})$ or the $N(\mathbf{0})\pi(\mathbf{0})\pi(\mathbf{0})$ state, and a width of 0.04–0.05 in lattice units.[1] The masses of these two states are roughly equal for the seven ensembles and lower than the M_1 obtained from the $\{4\}$ fit. The lower energy $N(-\mathbf{1})\pi(\mathbf{1})$ state has been shown to contribute in the axial channel [36], whereas for the vector channel the $N(\mathbf{0})\pi(\mathbf{0})\pi(\mathbf{0})$ state is expected to be the relevant one based on vector meson dominance. Since the two states have roughly the same mass, which is all that matters in the fits, we do not distinguish between them and use the common label $\{4^{N\pi}\}$. We also emphasize that even though we use a Bayesian procedure for stabilizing the fits, the errors are calculated using the jackknife method and are thus the usual frequentist standard errors.

In the fits to the two-point functions, the $\{4\}$ and $\{4^{N\pi}\}$ strategies cannot be distinguished on the basis of the χ^2/dof. In fact, the full range of M_1 values between the two estimates, from $\{4\}$ and $\{4^{N\pi}\}$, are viable on the basis of χ^2/dof alone. The same is true of the values for M_2, indicating a large flat region in parameter space. Because of this large region of possible values for the excited-state masses, M_i, we carry out the full analysis with three strategies that use different estimates of M_i and investigate the sensitivity of the results on them. The ground-state nucleon mass obtained from the $\{4\}$ and $\{4^{N\pi}\}$ fits is denoted by the common symbol $M_N \equiv M_0$ and the successive mass gaps by $\Delta M_i \equiv M_i - M_{i-1}$. These are given in table 3, and in tables 7, 8 and 9 in appendix B.

[1] When priors are used, the augmented χ^2 is defined as the standard correlated χ^2 plus the square of the deviation of the parameter from the prior mean normalized by the prior width. This quantity is minimized in the fits. In the following we quote this augmented χ^2 divided by the degrees of freedom calculated without reference to the prior, and call it χ^2/dof for brevity. In cases where the prior is used only to stabilize the fit, ie, with large width, the latter is a small correction to the standard χ^2.

JHEP04(2021)044

The analysis of the three-point functions, $C_{\mathcal{O}}^{\rm 3pt}$, with insertion of zero-momentum operators defined in eqs. (3.5), (3.6) and (3.7), is performed retaining up to three states $|i\rangle$ in the spectral decomposition:

$$C_{\mathcal{O}}^{\rm 3pt}(\tau;t) = \sum_{i,j=0}^{2} |\mathcal{A}_i||\mathcal{A}_j|\langle i|\mathcal{O}|j\rangle e^{-M_i t - M_j(\tau-t)} \,. \tag{5.2}$$

To get the forward matrix element, we fix the momentum at the sink to zero. To remove the ESC and extract the desired ground-state matrix element, $\langle 0|\mathcal{O}|0\rangle$, we make a simultaneous fit in t and τ. The full set of values of τ investigated are given in table 1. In choosing the set of points, $\{t,\tau\}$, to include in the final fit, we attempt to balance statistical and systematic errors. First, we neglect $t_{\rm skip}$ points next to the source and sink in the fits as these have the largest ESC. Next, noting that the data at smaller τ have exponentially smaller errors but larger ESC, we pick the largest three values of τ for all seven ensembles. Since errors in the data grow with τ, we partially compensate for the larger weight given to smaller τ data by choosing $t_{\rm skip}$ to be the same for all τ, i.e., by including increasingly more t points with larger τ, the weight of the larger τ data points is increased. Most of our analysis uses a 3*-fit, which is a three-state fit with the term involving $\langle 2|\mathcal{O}|2\rangle$ set to zero, as it is essentially undetermined and its inclusion results in an overparameterization based on the Akaike information criteria [37].

The key challenge to 3-state fits using eq. (5.2) to control ESC is determining the relevant M_i to use because fits to the two-point function show a large flat region in the space of the M_i with roughly the same χ^2/dof. Theoretically, there are many candidate intermediate states, and their contribution to the three-point functions with the insertion of operator $\mathcal{O}$ is not known *a priori*. Assuming the lattice theory has a discrete spectra in a finite box, the key parameter is the mass gap ΔM_1 of the first excited state that provides the dominant contribution. Theoretically, the lightest possible state with positive parity contributing to the forward matrix elements is either $N(\boldsymbol{p}=1)\pi(\boldsymbol{p}=-1)$ or $N(0)\pi(0)\pi(0)$ depending on the value of M_π and the lowest momenta, which is larger than 200 MeV on all seven ensembles. For our ensembles, the non-interacting energies for these two states are roughly equal. We subsume both possibilities by the common label $N\pi$. Thus in the strategy $\{4^{N\pi}, 3^*\}$, ΔM_1 is approximately the lowest possible value, and corresponds to the case that one (or both) of these states gives the dominant ESC.

To investigate the sensitivity of $\langle 0|\mathcal{O}|0\rangle$ to possible values of M_i, we carry out the full analysis with the following three strategies using the mnemonic $\{m,n\}$ to denote an m-state fit to the two-point function and an n-state fit to the three-point function:

- $\{4, 3^*\}$: the spectrum is taken from a $\{4\}$ state fit to the two-point function using eq. (5.1) and then a $\{3^*\}$ fit is made to the three-point function using eq. (5.2). Both fits are made within a single jackknife loop. This is the standard strategy, which assumes that the same set of states are dominant in the two- and three-point functions.
- $\{4^{N\pi}, 3^*\}$: the excited state spectrum is taken from a four-state fit to the two-point function but with a narrow prior for the first excited state mass taken to be the energy of a non-interacting $N(\boldsymbol{p}=1)\pi(\boldsymbol{p}=-1)$ state (or $N(0)\pi(0)\pi(0)$, which has

JHEP04(2021)044

roughly the same energy). This spectrum is then used in a $\{3^*\}$ fit to the three-point function. This variant of the $\{4, 3^*\}$ strategy assumes that the lowest of the theoretically allowed tower of $N\pi$ (or $N\pi\pi$) states contributes.

- $\{4, 2^{\text{free}}\}$: the only parameters taken from the $\{4\}$ state fit are the ground state amplitude $\mathcal{A}_0$ and mass M_0, whose determination is robust — the variation in M_0 between $\{4, 3^*\}$ and $\{4^{N\pi}, 3^*\}$ is $\lesssim 1\%$ as shown in table 3. In the two-state fit to the three-point function, the mass of the first excited state, M_1, is left as a free parameter, ie, the most important determinant of ESC, M_1, is obtained from the fit to the three-point function. The relative limitation of the $\{4, 2^{\text{free}}\}$ strategy is that, with the current data, we can only make two-state fits to the three-point functions, ie, include only one excited state.

The data for the ratios $R_{\mathcal{O}}(\tau; t)$ are plotted in figures 5–10 in appendix A for the three operators, the three strategies, and all seven ensembles. We note the following features:

- The fractional statistical errors are less than 2% for all three operators and on all seven ensembles. The only exceptions are the $\tau = 16$ ($\tau = 21$) data on the $a094m270$ and $a091m170L$ ($a071m170$) ensembles.
- The errors grow, on average, by a factor between 1.3–1.5 for every two units increase in τ/a. This is smaller than the asymptotic factor, $e^{(M_N - 3M_\pi/2)\tau}$, expected for nucleon correlation functions. There is also a small increase in this factor between $\langle x \rangle_{u-d} \to \langle x \rangle_{\Delta u - \Delta d} \to \langle x \rangle_{\delta u - \delta d}$.
- The data for all three operators is symmetric about $t = \tau/2$ as predicted by the spectral decomposition. Only on three ensembles, $a094m270$, $a091m170L$ and $a071m170$, the symmetry about $t = \tau/2$ is not manifest in the largest τ data. As stated above, these data have the largest errors, moreover the deviations are within errors.
- In all cases (operators and ensembles), the convergence of the data towards the $\tau \to \infty$ value is monotonic and from above. Thus, ESC causes all three moments to be overestimated.

With the data satisfying the expected conditions, we make the three fits, $\{4, 3^*\}$, $\{4^{N\pi}, 3^*\}$ and $\{4, 2^{\text{free}}\}$, to the largest three values of τ in all cases. We have also checked that the results from fits keeping the largest four values of τ overlap with these within 1σ. The result of the fit and the $\tau = \infty$ value (blue band) are shown in each panel in figures 5–10. The three panels in each row of the figures have the same data but show fits with the three strategies that are being compared. The ensemble ID, the value of the unrenormalized moment obtained using eqs. (3.8), or (3.9), or (3.10), the χ^2/dof of the fit, and the values of τ for which the data are shown are also given in the figure labels. The scale for the y-axis is chosen to be the same for all the plots to facilitate comparison.

The values of ΔM_1 entering/determined by the various fits are given in table 3. They display the following qualitative features:

- The values $a\Delta M_1^{\{4\}} \approx 0.6 a M_N^{\{4\}}$. This suggests that the lowest excited state in the $\{4\}$ fit to the two-point function is close to the $N(1440)$.

JHEP04(2021)044

- $a\Delta M_1^{\{4^{N\pi}\}}$ is significantly smaller than $a\Delta M_1^{\{4\}}$ as mentioned above.
- On five ensembles, $a\Delta M_1^{\{2^{\text{free}}\}}$ from fits to the momentum-fraction data are consistent with $a\Delta M_1^{\{2\}}$. (table 3 gives both $a\Delta M_1^{\{2\}}$ and $a\Delta M_1^{\{4\}}$ to show the variation between a two- and four-state fit.) To check whether this rough agreement is a possibility for the remaining two ensembles, $a094m270$ and $a071m170$, we made fits with a range of priors but did not find a flat direction with respect to $a\Delta M_1^{\{2^{\text{free}}\}}$. Thus, the large values of $a\Delta M_1^{\{2^{\text{free}}\}}$ from these two ensembles are unexplained, however, as noted previously, the statistical errors in these two ensembles are the largest.
- The $a\Delta M_1^{\{2^{\text{free}}\}}$ for helicity and transversity moments are roughly the same and much larger than even $a\Delta M_1^{\{2\}}$.

The results for the unrenormalized moments obtained using eqs. (3.8), or (3.9), or (3.10) are given in table 6 along with the values of t_{skip} used. The parameters and the χ^2/dof of the fits for the various strategies are given in tables 7, 8, and 9 in appendix B. In these tables, we include results with $\{4, 2\}$ and $\{4^{N\pi}, 2\}$ strategies in addition to the $\{4, 3^*\}$, $\{4^{N\pi}, 3^*\}$ and $\{4, 2^{\text{free}}\}$ to show that the variation on including the second excited state is small, ie, ΔM_1 is the dominant parameter in controlling ESC.

We draw the following conclusions from the results presented in tables 3– 9 and the fits shown in figures 5–10:

- The statistics on the $a091m170L$ and $a071m170$ ensembles need to be increased further as they control the chiral extrapolation in the CCFV fits.
- The χ^2/dof of most fits are reasonable.
- The $\{4, 2^{\text{free}}\}$ fits have reasonable χ^2/dof but do not indicate a preference for the small $\Delta M_1^{N\pi}$ given in table 3. Their ΔM_1 lie closer to or higher than $\Delta M_1^{\{2\}}$.
- The ΔM_1 from a two-state fit is expected to be larger since it is an effective combination of the mass gaps of the full tower of excited states. This is illustrated by the difference between $\Delta M_1^{\{2\}}$ and $\Delta M_1^{\{4\}}$. Thus we take the values $\Delta M_1^{\{4^{N\pi}\}}$ and $a\Delta M_1^{\{2^{\text{free}}\}}$ to bracket possible values of ΔM_1 in each case.

Based on the above arguments, we will choose the $\{4, 3^*\}$ results obtained after performing the CCFV fits for the final central value. We will also assign half the spread between the $\{4^{N\pi}, 3^*\}$ and $\{4, 2^{\text{free}}\}$ values as a second uncertainty to account for possible unresolved ESC.

To get the renormalized values of the moments, the renormalization factors, Z_{VD}, Z_{AD}, and Z_{TD}, are calculated on the lattice in the RI′−MOM scheme and then converted to the $\overline{\text{MS}}$ scheme at 2 GeV. Two methods to control discretization errors in the calculation of the Z's are described in appendix C. The final values of Z_{VD}, Z_{AD}, and Z_{TD} used in the analysis are given in table 10. The values of the three renormalized moments from the seven ensembles and with the three strategies are summarized in table 11 for renormalization method A and in table 12 for method B in appendix C. These data are used to perform the CCFV fits discussed next.

JHEP04(2021)044

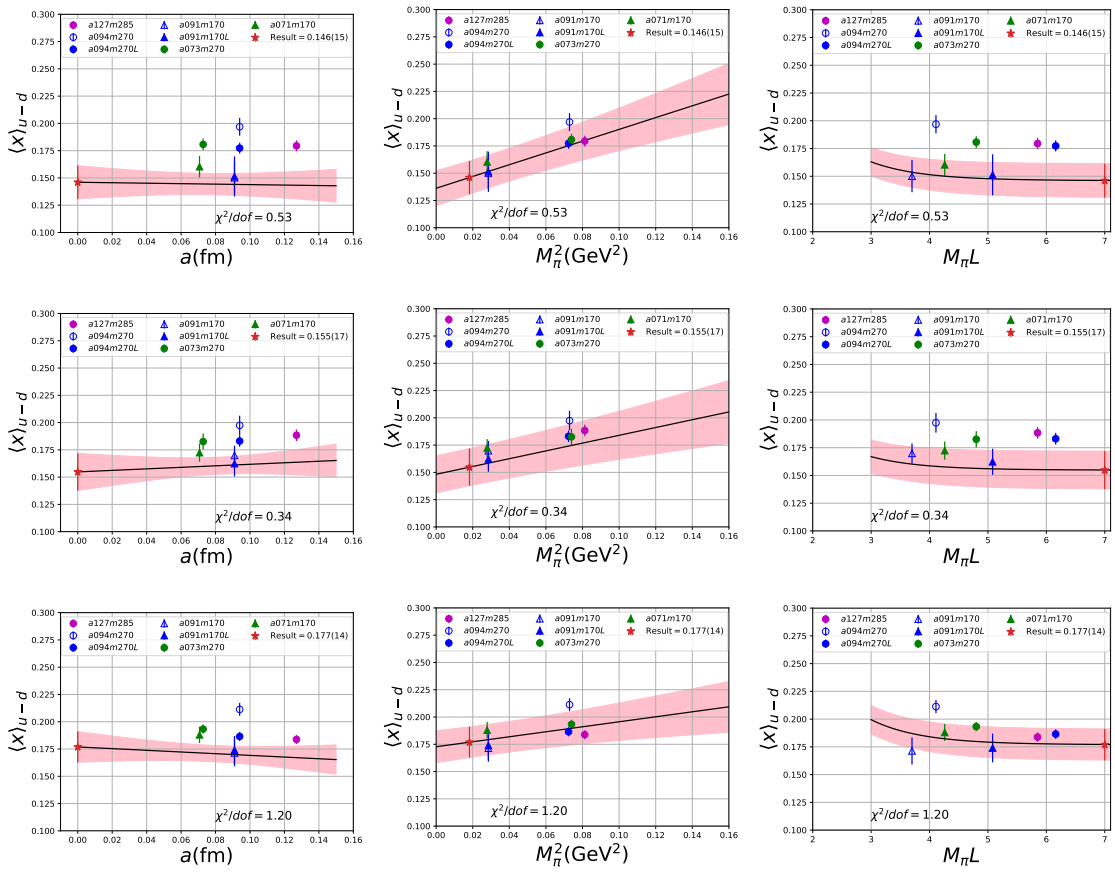

Figure 1. Data for the momentum fraction $\langle x \rangle_{u-d}$ from the seven ensembles renormalized using method A in the $\overline{\text{MS}}$ scheme at $\mu = 2\,\text{GeV}$. The top row shows data obtained using the $\{4^{N\pi}, 3^*\}$ fits strategy, middle from $\{4, 3^*\}$ and bottom from $\{4, 2^{\text{free}}\}$. The pink band shows the result of the CCFV fit plotted versus a (left panel), versus M_π^2 (middle panel) and versus $M_\pi L$ (right panel) with the other two variables set to their physical values in each case. The desired value at the physical point is shown by the symbol red star. Note that, since we do not shift the data to account for the corrections due to the other two variables in each panel, the data and the result of the simultaneous fit (pink band with central value given by the black line) are not expected to coincide. By presenting unshifted data, we allow the reader to see the size of the corrections due to extrapolation in the other two variables, ie, roughly the difference between the data point and the central value given by the fit. The χ^2/dof show that the fits are reasonable.

JHEP04(2021)044

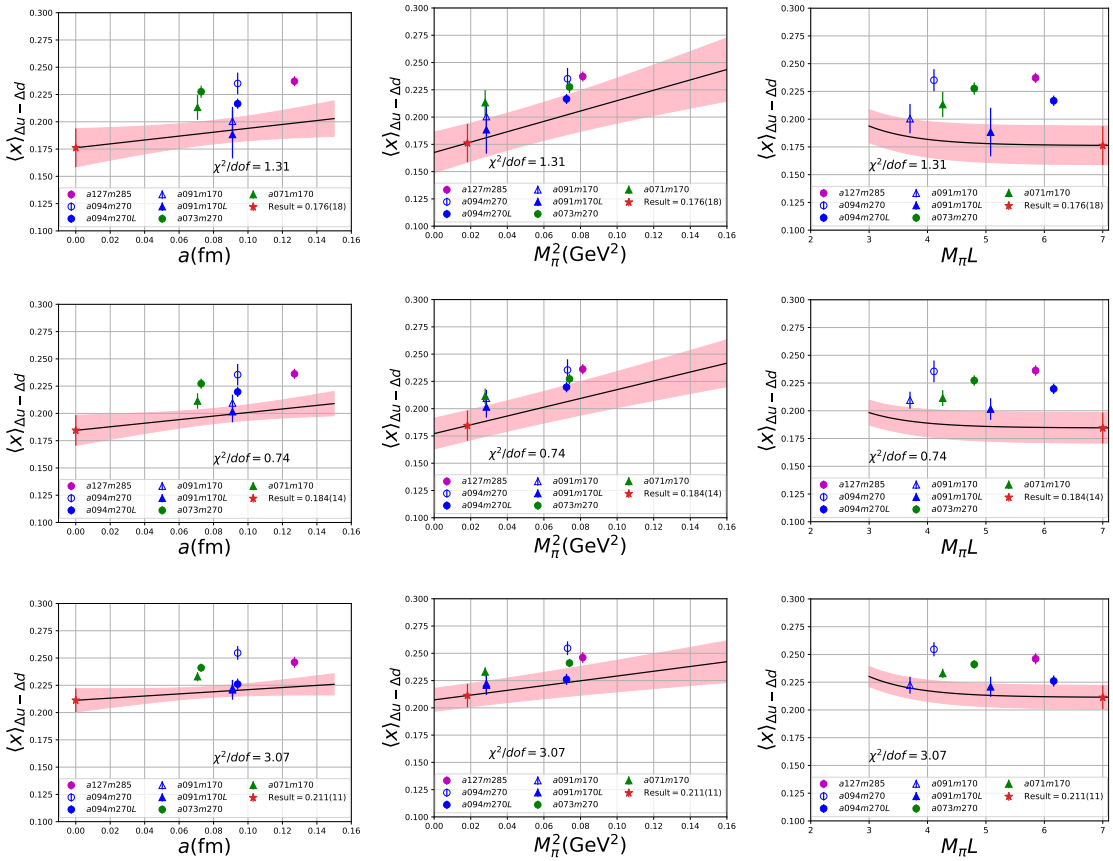

Figure 2. Data for the helicity moment $\langle x \rangle_{\Delta u - \Delta d}$ from the seven ensembles renormalized using method A in the $\overline{\text{MS}}$ scheme at $\mu = 2\,\text{GeV}$. The rest is the same as in figure 1.

JHEP04(2021)044

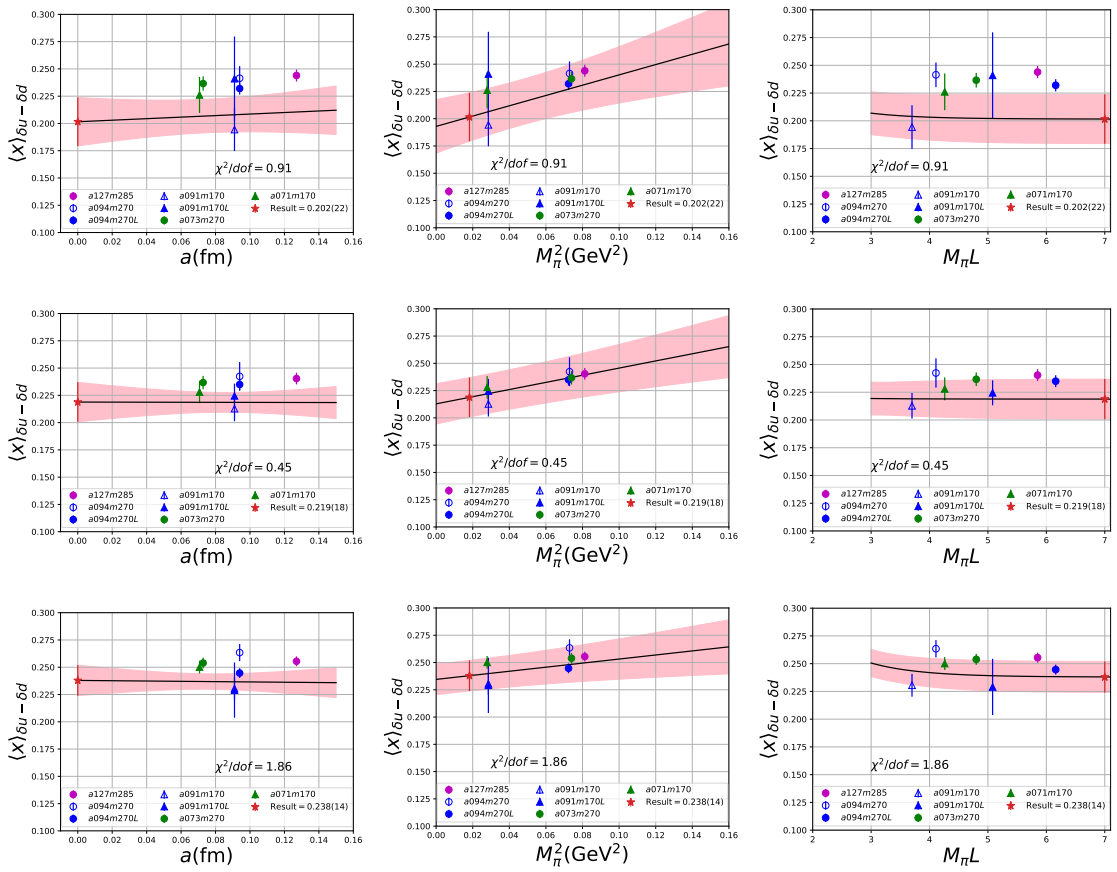

Figure 3. Data for the transversity moment $\langle x \rangle_{\delta u - \delta d}$ from the seven ensembles renormalized using method A in the $\overline{\text{MS}}$ scheme at $\mu = 2\,\text{GeV}$. The rest is the same as in figure 1.

6 Chiral, continuum and infinite volume extrapolation

To obtain the final, physical results at $M_\pi = 135\,\text{MeV}$, $M_\pi L \to \infty$ and $a = 0$, we make a simultaneous CCFV fit keeping only the leading correction term in each variable:

$$\langle x \rangle(M_\pi; a; L) = c_1 + c_2 a + c_3 M_\pi^2 + c_4 \frac{M_\pi^2\, e^{-M_\pi L}}{\sqrt{M_\pi L}}\,. \tag{6.1}$$

Note that, since the operators are not $O(a)$ improved in our clover-on-clover formulation, we take the discretization errors to start with a term linear in a. The fits to the data renormalized using method A for the three strategies are shown in figures 1, 2 and 3 and the results are summarized in table 4.

The dependence on a is found to be small. The significant variation is with M_π^2, and this is the main discriminant between the three strategies. The smaller the ΔM_1, the larger is the extrapolation in the ESC fits (difference between the data at the largest τ and the $\tau = \infty$ extrapolated value). Since the difference in the ΔM_1 is M_π dependent, it, in turn, leads to a larger slope versus M_π^2 in the CCFV fits. The overall consequence for all three moments is that estimates increase by about 0.02 at each step, $\{4^{N\pi}, 3^*\} \to \{4, 3^*\} \to$

JHEP04(2021)044

strategy	Renorm Method	$\langle x \rangle_{u-d}$ CC	$\langle x \rangle_{u-d}$ CCFV	$\langle x \rangle_{\Delta u-\Delta d}$ CC	$\langle x \rangle_{\Delta u-\Delta d}$ CCFV	$\langle x \rangle_{\delta u-\delta d}$ CC	$\langle x \rangle_{\delta u-\delta d}$ CCFV
$\{4^{N\pi}, 3^*\}$	A	0.161(13)	0.146(15)	0.192(15)	0.176(18)	0.207(19)	0.202(22)
$\{4^{N\pi}, 3^*\}$	B	0.161(12)	0.147(15)	0.191(15)	0.174(17)	0.210(19)	0.204(22)
$\{4^{N\pi}, 3^*\}$	Final	0.161(13)	0.147(15)	0.192(15)	0.175(18)	0.209(19)	0.203(22)
$\{4, 3^*\}$	A	0.165(15)	0.155(17)	0.197(11)	0.184(14)	0.219(15)	0.219(18)
$\{4, 3^*\}$	B	0.164(15)	0.154(16)	0.195(11)	0.182(14)	0.222(15)	0.221(18)
$\{4, 3^*\}$	Final	0.165(15)	0.155(17)	0.196(11)	0.183(14)	0.221(15)	0.220(18)
$\{4, 2^{\text{free}}\}$	A	0.195(13)	0.177(14)	0.2266(90)	0.211(11)	0.248(12)	0.238(14)
$\{4, 2^{\text{free}}\}$	B	0.194(13)	0.177(14)	0.2228(93)	0.206(11)	0.248(12)	0.237(14)
$\{4, 2^{\text{free}}\}$	Final	0.195(13)	0.177(14)	0.2247(93)	0.209(11)	0.248(12)	0.238(14)

Table 4. The final results of the chiral-continuum-finite-volume fits for the three moments and the three strategies used to remove excited state contamination. Results are given for the two methods of renormalization (A and B) discussed in appendix C. The final value for each strategy is taken to be the average of the two estimates along with the larger of the two errors.

$\{4, 2^{\text{free}}\}$. Based on the observation that the $\{4, 2^{\text{free}}\}$ fits do not prefer the small $\Delta M_1^{\{4^{N\pi}\}}$, but are closer to $\Delta M_1^{\{2\}}$ (momentum fraction) or larger (helicity and transversity), we take the $\{4, 3^*\}$ results as our best estimates. However, to account for possible bias due to not having resolved which excited state gives the dominant contribution, we add a second, systematic, error of 0.02 to the final results based on the observed differences in estimates between the three strategies.

The results from the two renormalization methods, summarized in table 4, overlap — the differences ($\lesssim 1\%$) are a fraction of the errors from the rest of the analysis. Also, note that these differences are much smaller than the differences between the Z's from the two methods given in table 10. This pattern is expected provided the differences in the Z's are largely due to discretization errors that are removed on taking the continuum limit.

Lastly, a comparison between the chiral-continuum (CC) and CCFV fit results summarized in table 4 indicate up to 10% decrease due to the finite volume correction term, however, this is comparable to the size of the final errors. Also, this effect is clear only between the $a094m270$ and $a094m270L$ data as shown in tables 11 and 12. Consequently, most of the variation versus $M_\pi L$ in the CCFV fit occurs for $M_\pi L < 4$. The result of a CC fit to five larger volume ensembles (excluding $a094m270$ and $a091m170$) lie in between the CC and CCFV data shown in tables 11 and 12, ie, well within the quoted 1σ error. With these caveats, for present, we choose to present final results from the full data set using CCFV fits.

JHEP04(2021)044

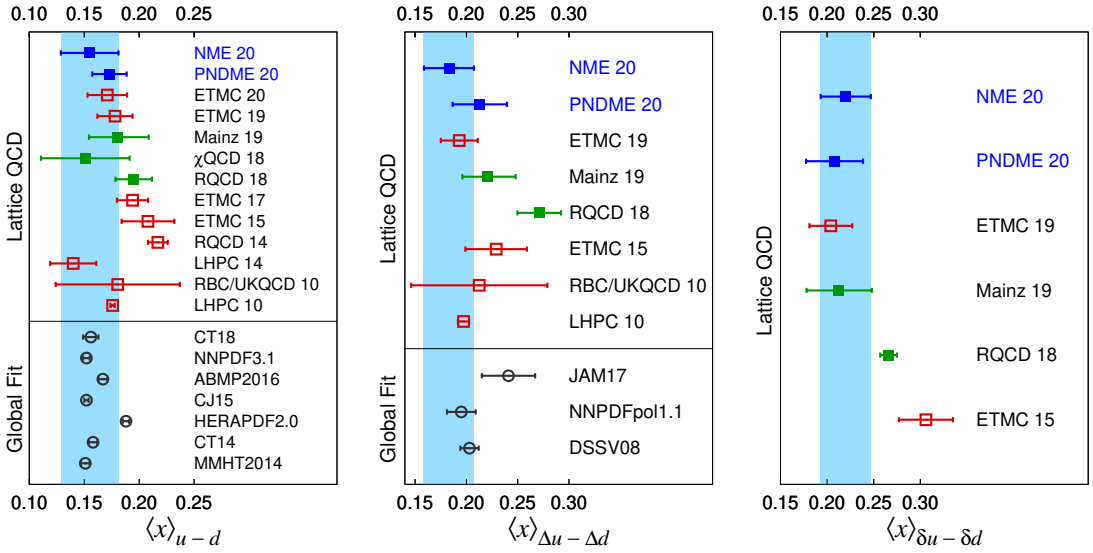

Figure 4. A comparison of results from lattice QCD calculations with dynamical fermions and global fits (below the black line) summarized in table 5. The left panel compares results for the momentum fraction, the middle for the helicity moment, and the right for the transversity moment. Our NME 20 result is also shown as the blue band to facilitate comparison.

With the above choices, our final results are

$$\begin{aligned} \langle x \rangle_{u-d} &= 0.155(17)(20)\,, \\ \langle x \rangle_{\Delta u - \Delta d} &= 0.183(14)(20)\,, \\ \langle x \rangle_{\delta u - \delta d} &= 0.220(18)(20)\,. \end{aligned} \tag{6.2}$$

We update the comparison of lattice QCD calculations on ensembles with dynamical fermions presented in ref. [16] in the top half of table 5 and in figure 4. Our new results, eq. (6.2), are consistent with the PNDME 20 values published in ref. [16]. This is a valuable check of the PNDME 20 calculation that uses the nonunitary clover-on-HISQ lattice formulation. A large part of the difference is due to the weak evidence for a finite-volume effect in the current calculation: the PNDME 20 results were obtained using just CC fits. On the other hand, the range of lattice spacings and pion masses simulated is somewhat smaller than in the PNDME 20 calculation.

Our result for the momentum fraction is in very good agreement with estimates from phenomenological global fits reviewed in ref. [11], summarized in the bottom half of table 5, and shown in figure 4. The helicity moment is consistent with the smaller error global fit values, and our transversity moment is a prediction.

7 Conclusions

We have presented results for the isovector quark momentum fraction, $\langle x \rangle^{\overline{\rm MS}}_{u-d}$, helicity moment, $\langle x \rangle^{\overline{\rm MS}}_{\Delta u - \Delta d}$, and transversity moment, $\langle x \rangle^{\overline{\rm MS}}_{\delta u - \delta d}$ on seven ensembles with 2+1-flavor Wilson-clover fermions. The high statistics data were essential for achieving the following five improvements.

JHEP04(2021)044

Collaboration	Ref.	$\langle x \rangle_{u-d}$	$\langle x \rangle_{\Delta u - \Delta d}$	$\langle x \rangle_{\delta u - \delta d}$	Remarks
NME 20 (this work)		0.155(17)(20)	0.183(14)(20)	0.220(18)(20)	$N_f = 2+1$ clover-on-clover
PNDME 20	[16]	0.173(14)(07)	0.213(15)(22)	0.208(19)(24)	$N_f = 2+1+1$ clover-on-HISQ
ETMC 20	[38]	0.171(18)			$N_f = 2+1+1$ Twisted Mass N-DIS, N-FV
ETMC 19	[39]	0.178(16)	0.193(18)	0.204(23)	$N_f = 2+1+1$ Twisted Mass N-DIS, N-FV
Mainz 19	[32]	$0.180(25)_{\text{stat}}$ $(+14,-6)_{\text{sys}}$	$0.221(25)_{\text{stat}}$ $(+10,-0)_{\text{sys}}$	$0.212(32)_{\text{stat}}$ $(+20,-10)_{\text{sys}}$	$N_f = 2+1$ Clover
χQCD 18	[40]	0.151(28)(29)			$N_f = 2+1$ Overlap on Domain Wall
RQCD 18	[41]	0.195(07)(15)	0.271(14)(16)	0.266(08)(04)	$N_f = 2$ Clover
ETMC 17	[42]	0.194(9)(11)			$N_f = 2$ Twisted Mass N-DIS, N-FV
ETMC 15	[43]	0.208(24)	0.229(30)	0.306(29)	$N_f = 2$ Twisted Mass N-DIS, N-FV
RQCD 14	[34]	0.217(9)			$N_f = 2$ Clover N-DIS, N-CE, N-FV
LHPC 14	[44]	0.140(21)			$N_f = 2+1$ Clover N-DIS ($a \sim 0.12$ fm)
RBC/ UKQCD 10	[45]	0.124–0.237	0.146–0.279		$N_f = 2+1$ Domain Wall N-DIS, N-CE, N-ES
LHPC 10	[46]	0.1758(20)	0.1972(55)		$N_f = 2+1$ Domain Wall-on-Asqtad N-DIS, N-CE, N-NR, N-ES
CT18	[47]	0.156(7)			
JAM17†	[11, 48]		0.241(26)		
NNPDF3.1	[49]	0.152(3)			
ABMP2016	[50]	0.167(4)			
CJ15	[51]	0.152(2)			
HERAPDF2.0	[52]	0.188(3)			
CT14	[53]	0.158(4)			
MMHT2014	[54]	0.151(4)			
NNPDFpol1.1	[55]		0.195(14)		
DSSV08	[56, 57]		0.203(9)		

Table 5. Our lattice QCD results are compared with other lattice calculations with N_f flavors of dynamical fermions in rows 2–13, and with results from phenomenological global fits in the remainder of the table. In both cases, the results are arranged in reverse chronological order. All results are in the $\overline{\text{MS}}$ scheme at scale 2 GeV. For a discussion and comparison of lattice and global fit results up to 2020, see ref. [12] and also the comparison in [47] for $\langle x \rangle_{u-d}$. The JAM17† estimate for $\langle x \rangle_{\Delta u - \Delta d}$ is obtained from [11], where, as part of the review, an analysis was carried out using the data in [48]. The following abbreviations are used in the remarks column for various sources of systematic uncertainties in lattice calculations — DIS: discretization effects, CE: chiral extrapolation, FV: finite volume effects, NR: nonperturbative renormalization, ES: excited state contaminations. A prefix "N-" means that the systematic uncertainty was neither adequately controlled nor estimated.

JHEP04(2021)044

- Clear demonstration that, as predicted by the spectral decomposition, the data for the three point functions is symmetric about $\tau/2$ for each τ and converges monotonically in τ. This is shown in figures 5–10.

- A complete analysis with three estimates of excited state masses taken from the two-point function ($\{4, 3^*\}$), including the lowest energy $N\pi$ state allowed theoretically ($\{4^{N\pi}, 3^*\}$), and that determined from the three-point function ($\{4, 2^{\text{free}}\}$). All fits to remove the ESC were made using the full covariance matrix. The spread in results is used to assign a systematic uncertainty to account for possible residual excited-state bias.

- Finite volume corrections have been estimated for the first time and there is evidence that these could be as large as 10% on ensembles with $M_\pi L \lesssim 4$.

- The analysis has been done with two methods for removing discretization errors in the calculations of renormalization constants. The discussion in appendix C and the results in table 4 show that they give the same renormalized moments in the continuum limit.

- This clover-on-clover analysis removes the unquantified systematic due to using the non-unitary clover-on-HISQ formulation in the calculation presented in PNDME 20 [16]. While this systematic is expected to be smaller than the $\sim$ 10% errors in the current calculation, nevertheless, removing it is part of our overall goal of controlling all systematics.

To obtain the final result in the continuum limit, we fit the seven points using the ansatz in eq. (6.1) that includes the leading order terms in M_π, the lattice spacing a and the finite volume parameter $M_\pi L$. Having two pairs of points, $\{a094m270, a094m270L\}$ and $\{a091m170, a091m170L\}$, that differ only in the lattice volume, allowed us to quantify finite volume corrections in all three moments as shown in figures 1, 2 and 3. A comparison of the results with and without the finite-volume correction (CCFV versus CC) are shown in table 4. Based on this analysis, we present final results from the CCFV fits that are about 5% smaller than the CC-fit values for the momentum fraction and the helicity moment. These results are an improvement over the PNDME 20 [16] values, which used the non-unitary clover-on-HISQ lattice formulation and were obtained using just CC fits.

In appendix C, we describe two methods for removing the p_μ^2 dependent artifacts in the renormalization constants. The results for the moments from these two methods are summarized in table 4. The data show that after the continuum extrapolation (CCFV or CC fits), the two estimates overlap even though the renormalization constants themselves differ by $\approx 5\%$ as shown in table 10. The better agreement after the continuum extrapolation suggests that the main difference between Z's from the two methods are indeed discretization artifacts.

The data at three values of the lattice spacing shown in figures 1, 2 and 3 do not exhibit any significant dependence on the lattice spacing a. The main variation is with M_π^2, and its magnitude depends on the mass gap of the first excited state used in the analysis of the ESC. Since the mass gaps obtained from fits to the three-point functions ($\{4, 2^{\text{free}}\}$ strategy)

JHEP04(2021)044

do not prefer values corresponding to the lowest possible excitations ($N\pi$ states used in the $\{4^{N\pi}, 3^*\}$ strategy) but are closer to two-state fits to the two-point function (see table 3), we quote final results from the $\{4, 3^*\}$ strategy. We add a systematic error of 0.02, based on the observed spread (see table 4), to account for possible unresolved excited-state effects.

Our final results, taken from table 4, are given in eq. (6.2). These are compared with other lattice calculations and phenomenological global fit estimates in table 5 and figure 4. They are in good agreement with other recent lattice results from the PNDME [16], ETMC [38, 39], Mainz [32] and χQCD [40] collaborations. Our estimate for the momentum fraction is in good agreement with most global fit estimates but has much larger error. The three estimates for the helicity moment from global fits have a large spread, and our estimate is consistent with the smaller error estimates. Lattice estimates for the transversity moment are a prediction. Work is under progress to reduce the errors by simulating at additional values of $\{a, M_\pi\}$ and by increasing the statistics.

Acknowledgments

The calculations used the Chroma software suite [30]. This research used resources at (i) the National Energy Research Scientific Computing Center, a DOE Office of Science User Facility supported by the Office of Science of the U.S. Department of Energy under Contract No. DE-AC02-05CH11231; (ii) the Oak Ridge Leadership Computing Facility, which is a DOE Office of Science User Facility supported under Contract DE-AC05-00OR22725, and was awarded through the INCITE Program project PHY138 and ALCC program project LGT107; (iii) the USQCD Collaboration, which are funded by the Office of Science of the U.S. Department of Energy, and (iv) Institutional Computing at Los Alamos National Laboratory. T. Bhattacharya and R. Gupta were partly supported by the U.S. Department of Energy, Office of Science, Office of High Energy Physics under Contract No. DE-AC52-06NA25396. F. Winter is supported by the U.S. Department of Energy, Office of Science, Office of Nuclear Physics under contract DE-AC05-06OR23177. B. Joó is supported by the U.S. Department of Energy, Office of Science, under contract DE-AC05-06OR22725. We acknowledge support from the U.S. Department of Energy, Office of Science, Office of Advanced Scientific Computing Research and Office of Nuclear Physics, Scientific Discovery through Advanced Computing (SciDAC) program, and of the U.S. Department of Energy Exascale Computing Project. T. Bhattacharya, R. Gupta, S. Mondal, S. Park and B.Yoon were partly supported by the LANL LDRD program, and S. Park by the Center for Nonlinear Studies.

A Plots of the ratio $C^{\mathrm{3pt}}_{\mathcal{O}}(\tau; t)/C^{\mathrm{2pt}}(\tau)$

This appendix contains plots of the unrenormalized isovector moments, $\langle x\rangle_{u-d}$, $\langle x\rangle_{\Delta u-\Delta d}$, and $\langle x\rangle_{\delta u-\delta d}$, for the seven ensembles in figures 5–10. The data shown are the ratio $C^{\mathrm{3pt}}_{\mathcal{O}}(\tau; t)/C^{\mathrm{2pt}}(\tau)$ multiplied by the appropriate factor given in eqs. (3.8)– (3.10) to get the three $\langle x\rangle$. The three panels in each row show fits with the three strategies: $\{4^{N\pi}, 3^*\}$ (left), $\{4, 3^*\}$ (middle) and $\{4, 2^{\mathrm{free}}\}$ (right). The fits to $C^{\mathrm{3pt}}_{\mathcal{O}}(\tau; t)$ using eq. (5.2) are made keeping data at the largest three values of τ in all cases as discussed in section 5. The results of these fit are shown for various τ by lines with the same color as the data. In

JHEP04(2021)044

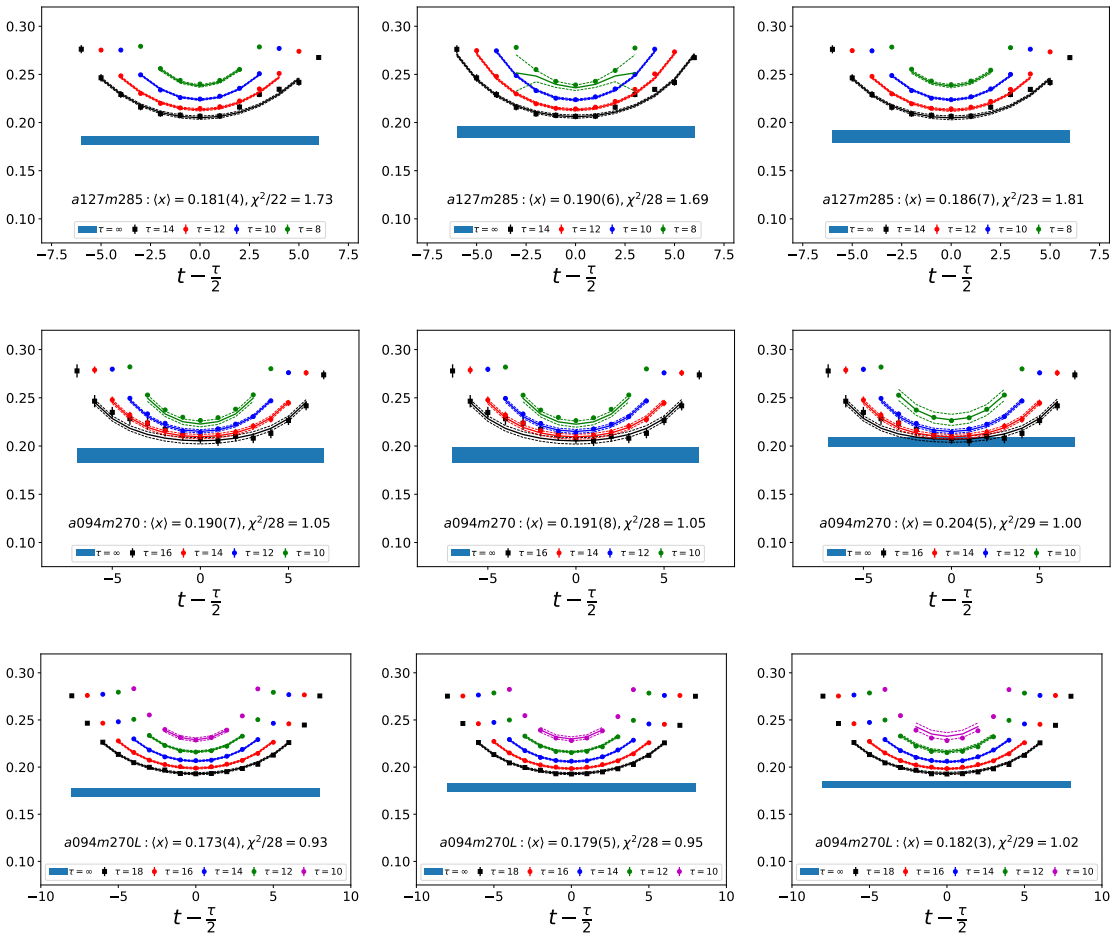

Figure 5. Data and fits to remove excited-state contamination in the extraction of the momentum fraction $\langle x \rangle_{u-d}$ for $a127m285$ (top row), $a094m270$ (middle row), and $a094m270L$ (bottom row) ensembles. The data for the ratio $C^{3\text{pt}}_{\mathcal{O}}(\tau;t)/C^{2\text{pt}}(\tau)$ is scaled using eq. (3.8) to give $\langle x \rangle_{u-d}$, and the fit parameters are listed in tables 7. In each row, the three panels show fits to the data with the largest three values of τ using the three strategies: $\{4^{N\pi}, 3^*\}$ (left), $\{4, 3^*\}$ (middle) and $\{4, 2^{\text{free}}\}$ (right). For each τ, the line in the same color as the data points is the result of the fit used (see section 5) to obtain the ground state matrix element. The result for the unrenormalized ground-state value of the moment is shown by the blue band and summarized in table 6 along with the values of t_{skip} used in the fit. The y-interval is selected to be the same for all the panels to facilitate comparison.

all cases, to extract the ground state matrix element (blue band), the fits to $C^{2\text{pt}}(\tau)$ and $C^{3\text{pt}}_{\mathcal{O}}(\tau;t)$ are done within a single jackknife loop.

The data show a monotonic convergence in τ towards the $\tau \to \infty$ estimate. Also, the data are symmetric about $t - \tau/2$ for all values of τ, except for the largest τ on the $a094m270$, $a091m170L$ and $a071m170$ ensembles, which are statistics limited. Lastly, the largest extrapolation, ie, the difference between the data at $t = \tau/2$ with the largest τ and the $\tau = \infty$ value, is for the $\{4^{N\pi}, 3^*\}$ strategy since it has the smallest mass gap as shown in table 3. This is most evident on the $M_\pi \approx 170\,\text{MeV}$ ensembles. The smallest is for the $\{4, 2^{\text{free}}\}$ strategy which has the largest mass gap.

JHEP04(2021)044

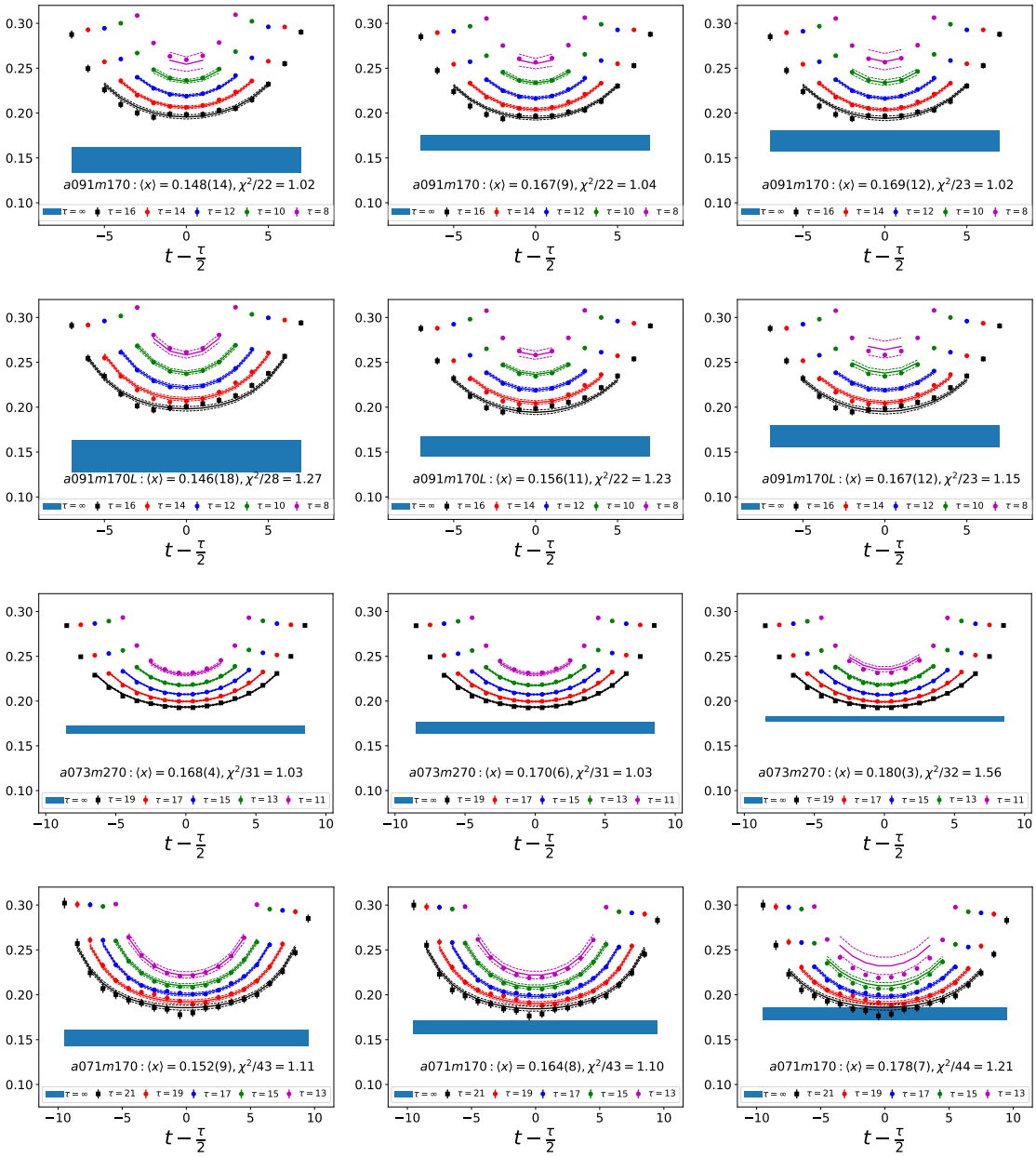

Figure 6. Continuation of the data and fits to remove excited-state contamination in the extraction of the momentum fraction $\langle x \rangle_{u-d}$ for $a091m170$ (top row), $a091m170L$ (second row), $a073m270$ (third row), and $a071m170$ (bottom row). The data for the ratio $C^{3\text{pt}}_{\mathcal{O}}(\tau;t)/C^{2\text{pt}}(\tau)$ is scaled using eq. (3.8) to give $\langle x \rangle_{u-d}$, and the fit parameters are listed in table 7. The rest is the same as in figure 5.

JHEP04(2021)044

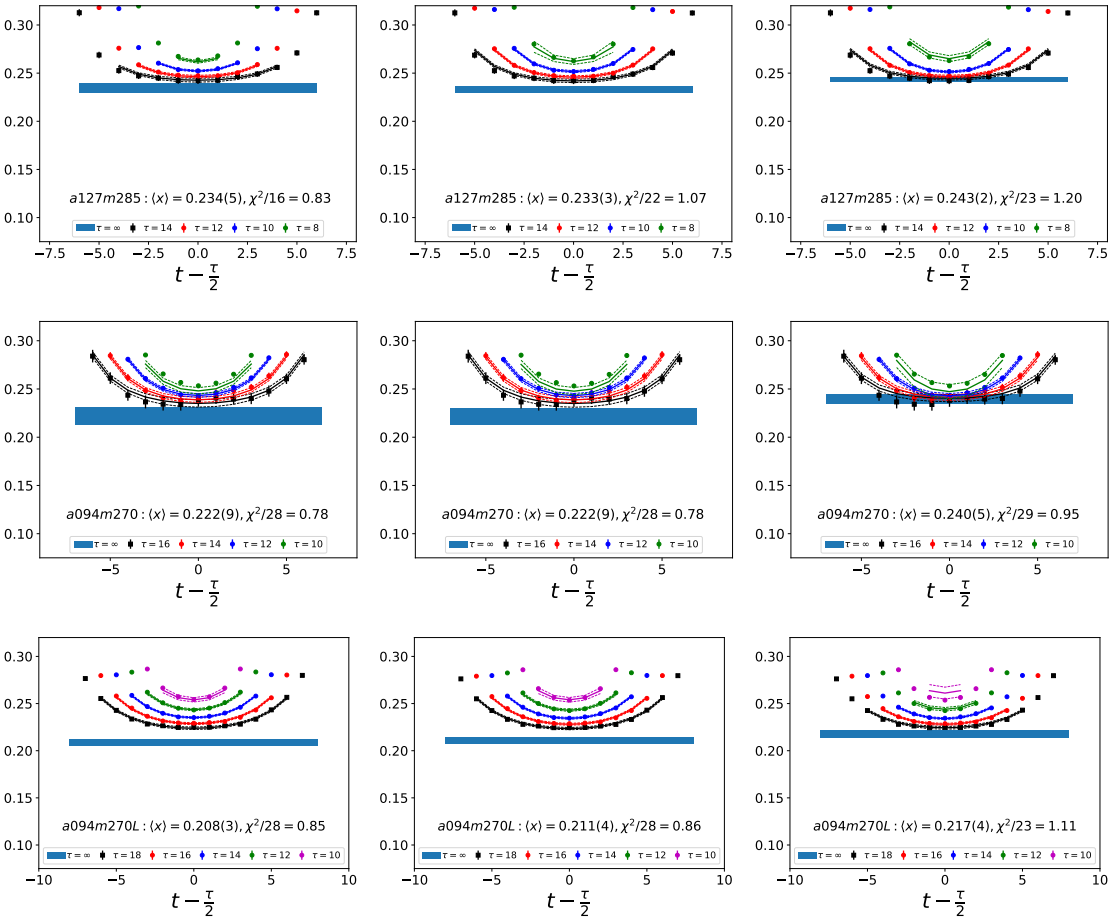

Figure 7. Data and fits to remove excited-state contamination in the extraction of the helicity moment $\langle x \rangle_{\Delta u - \Delta d}$ for $a127m285$ (top row), $a094m270$ (middle row), and $a094m270L$ (bottom row) ensembles. The data for the ratio $C^{3\text{pt}}_{\mathcal{O}}(\tau;t)/C^{2\text{pt}}(\tau)$ is scaled using eq. (3.9) to give $\langle x \rangle_{\Delta u - \Delta d}$, and the fit parameters are listed in table 8. The rest is the same as in figure 5.

JHEP04(2021)044

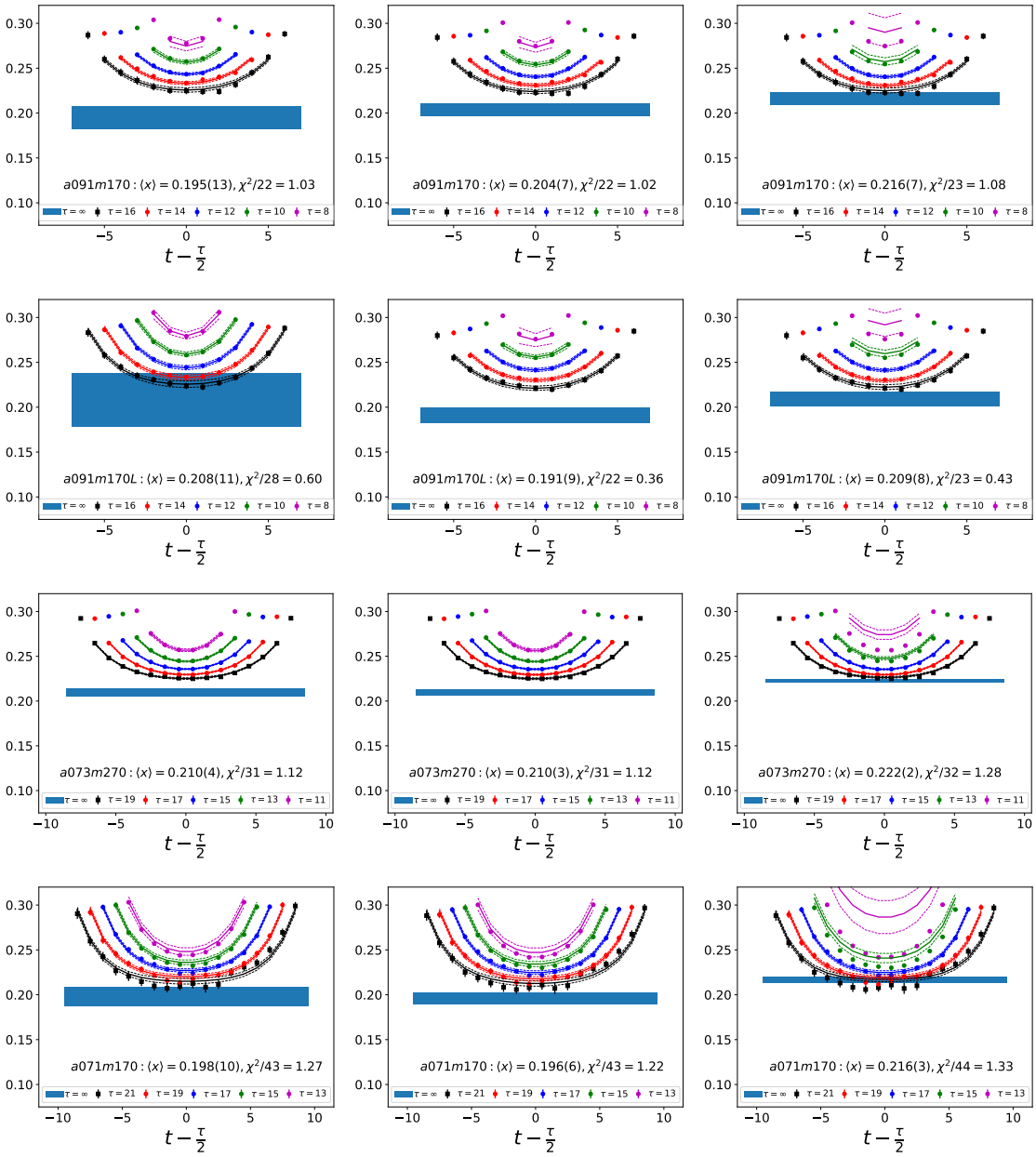

Figure 8. Continuation of the data and fits to remove excited-state contamination in the extraction of the helicity moment $\langle x \rangle_{\Delta u - \Delta d}$ for $a091m170$ (top row), $a091m170L$ (second row), $a073m270$ (third row), and $a071m170$ (bottom row). The data for the ratio $C^{3\text{pt}}_{\mathcal{O}}(\tau;t)/C^{2\text{pt}}(\tau)$ is scaled using eq. (3.9) to give $\langle x \rangle_{\Delta u - \Delta d}$, and the fit parameters are listed in table 8. The rest is the same as in figure 5.

JHEP04(2021)044

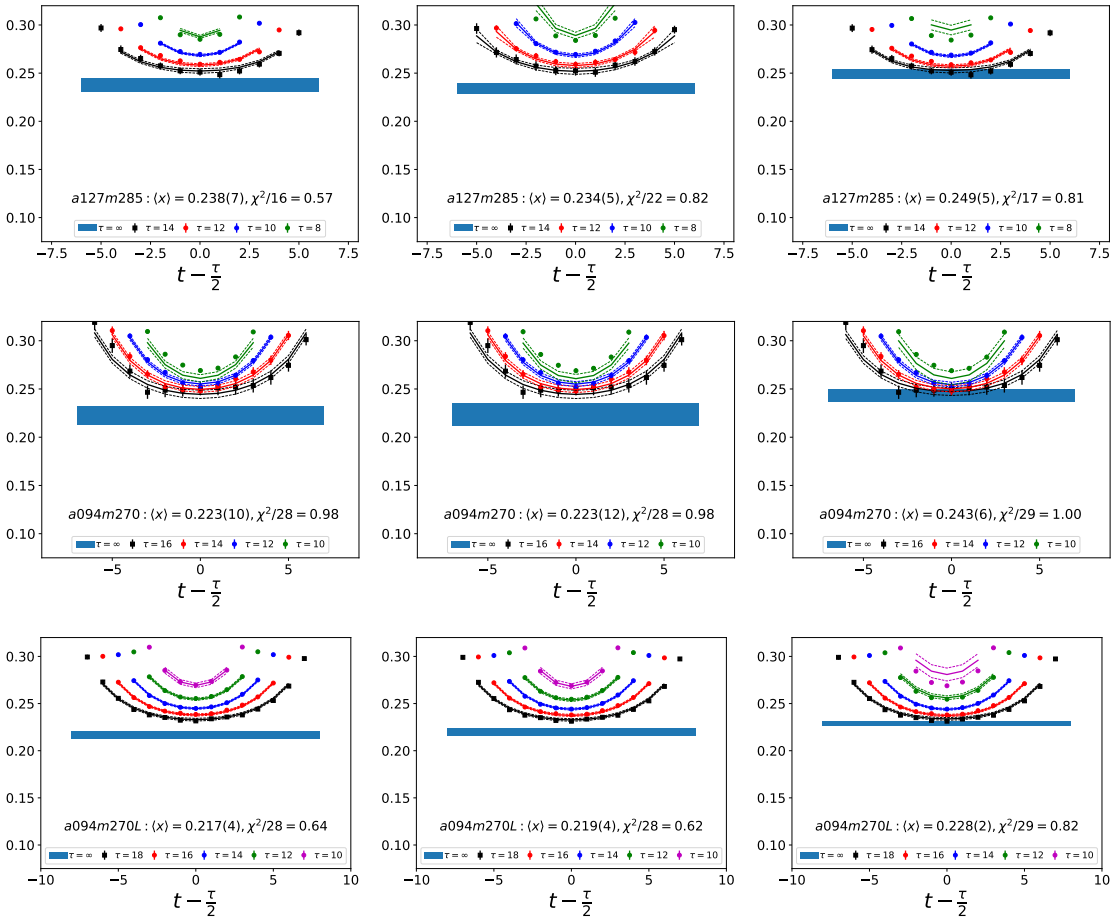

Figure 9. Data and fits to remove excited-state contamination in the extraction of the transversity moment $\langle x \rangle_{\delta u - \delta d}$ for $a127m285$ (top row), $a094m270$ (middle row), and $a094m270L$ (bottom row) ensembles. The data for the ratio $C^{3\text{pt}}_{\mathcal{O}}(\tau;t)/C^{2\text{pt}}(\tau)$ is scaled using eq. (3.10) to give $\langle x \rangle_{\delta u - \delta d}$, and the fit parameters are listed in table 9. The rest is the same as in figure 5.

JHEP04(2021)044

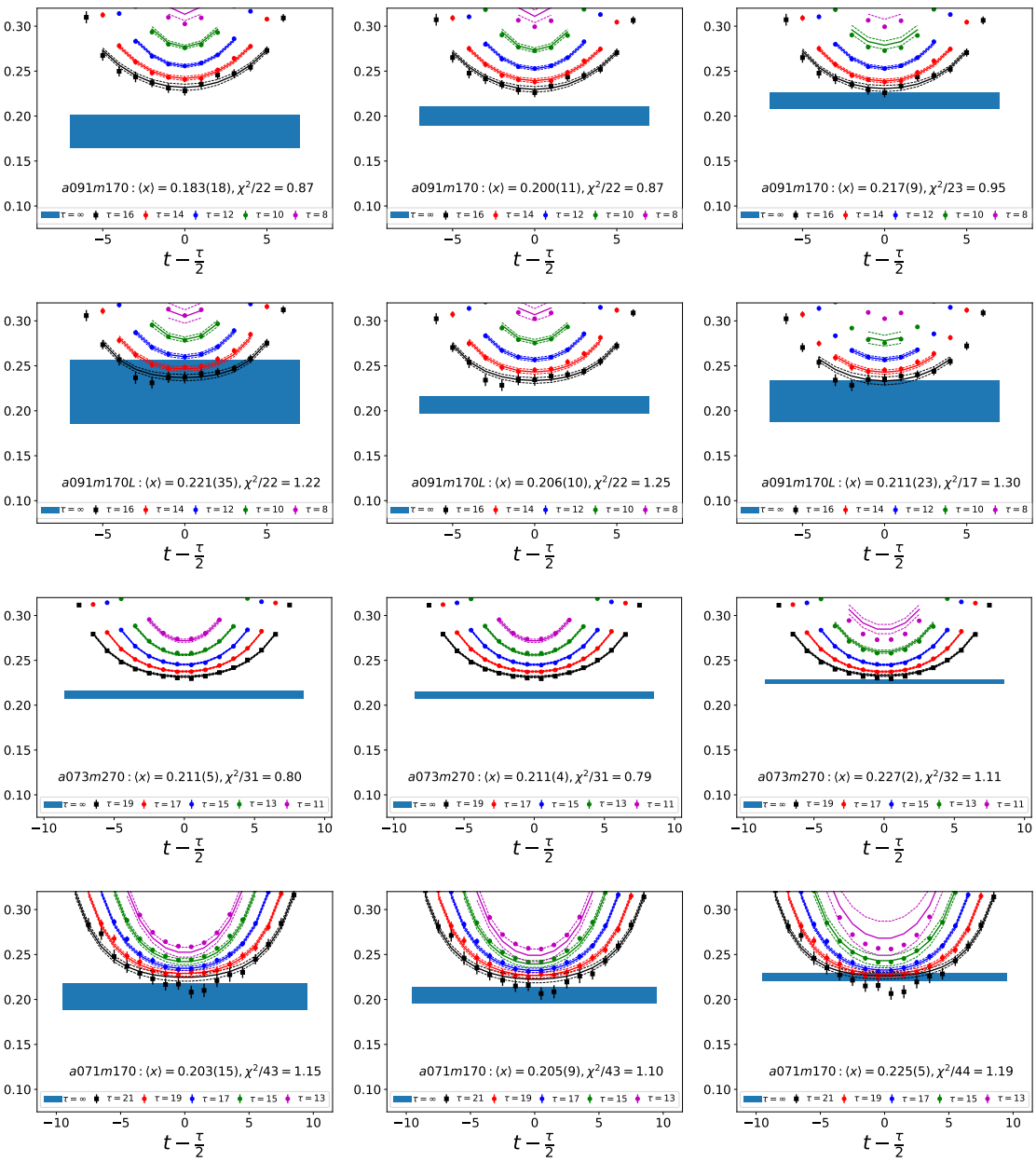

Figure 10. Continuation of the data and fits to remove excited-state contamination in the extraction of the transversity moment $\langle x \rangle_{\delta u - \delta d}$ for $a091m170$ (top row), $a091m170L$ (second row), $a073m270$ (third row), and $a071m170$ (bottom row). The data for the ratio $C^{3\text{pt}}_{\mathcal{O}}(\tau;t)/C^{2\text{pt}}(\tau)$ is scaled using eq. (3.10) to give $\langle x \rangle_{\delta u - \delta d}$, and the fit parameters are listed in table 9. The rest is the same as in figure 5.

JHEP04(2021)044

B Results of excited-state fits

This appendix provides the results of the fits used to remove the excited-state contamination. In table 6, we give the cuts on the data used in the fits (values of τ and t_{skip}), and the results for the unrenormalized moments. Tables 7, 8, and 9 give the values of the fit parameters defined in eq. (5.2) for the different strategies used for removing the excited-state contamination.

		$\{4^{N\pi}, 3^*\}$		$\{4, 3^*\}$		$\{4, 2^{\text{free}}\}$	
moment	τ fit	t_{skip}	$\langle x \rangle$	t_{skip}	$\langle x \rangle$	t_{skip}	$\langle x \rangle$
$a127m285$							
$\langle x \rangle_{u-d}$	$\{10, 12, 14\}$	2	0.181(4)	1	0.190(6)	2	0.186(7)
$\langle x \rangle_{\Delta u - \Delta d}$	$\{10, 12, 14\}$	3	0.234(5)	2	0.233(3)	2	0.243(2)
$\langle x \rangle_{\delta u - \delta d}$	$\{10, 12, 14\}$	3	0.238(7)	2	0.234(5)	3	0.249(5)
$a094m270$							
$\langle x \rangle_{u-d}$	$\{12, 14, 16\}$	2	0.190(7)	2	0.190(8)	2	0.203(5)
$\langle x \rangle_{\Delta u - \Delta d}$	$\{12, 14, 16\}$	2	0.222(9)	2	0.222(9)	2	0.240(5)
$\langle x \rangle_{\delta u - \delta d}$	$\{12, 14, 16\}$	2	0.222(10)	2	0.223(11)	2	0.243(6)
$a094m270L$							
$\langle x \rangle_{u-d}$	$\{14, 16, 18\}$	3	0.173(4)	3	0.179(5)	3	0.182(3)
$\langle x \rangle_{\Delta u - \Delta d}$	$\{14, 16, 18\}$	3	0.208(3)	3	0.211(4)	4	0.217(4)
$\langle x \rangle_{\delta u - \delta d}$	$\{14, 16, 18\}$	3	0.217(4)	3	0.219(4)	3	0.228(2)
$a091m170$							
$\langle x \rangle_{u-d}$	$\{12, 14, 16\}$	3	0.148(14)	3	0.167(9)	3	0.169(12)
$\langle x \rangle_{\Delta u - \Delta d}$	$\{12, 14, 16\}$	3	0.195(13)	3	0.204(7)	3	0.216(7)
$\langle x \rangle_{\delta u - \delta d}$	$\{12, 14, 16\}$	3	0.183(18)	3	0.200(11)	3	0.217(9)
$a091m170L$							
$\langle x \rangle_{u-d}$	$\{12, 14, 16\}$	2	0.146(18)	3	0.156(11)	3	0.167(12)
$\langle x \rangle_{\Delta u - \Delta d}$	$\{12, 14, 16\}$	3	0.178(21)	3	0.191(9)	3	0.209(9)
$\langle x \rangle_{\delta u - \delta d}$	$\{12, 14, 16\}$	3	0.221(35)	3	0.206(10)	4	0.211(23)
$a073m270$							
$\langle x \rangle_{u-d}$	$\{15, 17, 19\}$	3	0.168(4)	3	0.170(6)	3	0.180(3)
$\langle x \rangle_{\Delta u - \Delta d}$	$\{15, 17, 19\}$	3	0.210(4)	3	0.210(3)	3	0.222(2)
$\langle x \rangle_{\delta u - \delta d}$	$\{15, 17, 19\}$	3	0.211(5)	3	0.211(4)	3	0.227(2)
$a071m170$							
$\langle x \rangle_{u-d}$	$\{17, 19, 21\}$	2	0.152(9)	2	0.164(8)	3	0.178(7)
$\langle x \rangle_{\Delta u - \Delta d}$	$\{17, 19, 21\}$	2	0.198(10)	2	0.196(6)	2	0.216(3)
$\langle x \rangle_{\delta u - \delta d}$	$\{17, 19, 21\}$	2	0.203(15)	2	0.205(9)	2	0.225(5)

Table 6. Unrenormalized moments on the seven ensembles from the three fit strategies, $\{4^{N\pi}, 3^*\}$, $\{4, 3^*\}$ and $\{4, 2^{\text{free}}\}$, used to analyze the ESC in the three-point functions. For each fit strategy, we give the cuts on the data: the common values of τ used in the fits, and the number of time slices t_{skip} omitted next to the source and the sink.

JHEP04(2021)044

$\langle x \rangle_{u-d}$									
Ensemble	fit-type	$a\Delta M_1$	$a\Delta M_2$	$\langle 0\|\mathcal{O}\|0\rangle$	$\frac{\langle 1\|\mathcal{O}\|1\rangle \|A_1\|^2}{\langle 0\|\mathcal{O}\|0\rangle \|A_0\|^2}$	$\frac{\langle 1\|\mathcal{O}\|0\rangle \|A_1\|}{\langle 0\|\mathcal{O}\|0\rangle \|A_0\|}$	$\frac{\langle 2\|\mathcal{O}\|0\rangle \|A_2\|}{\langle 0\|\mathcal{O}\|0\rangle \|A_0\|}$	$\frac{\langle 2\|\mathcal{O}\|1\rangle \|A_2\|\|A_1\|}{\langle 0\|\mathcal{O}\|0\rangle \|A_0\|^2}$	χ^2/dof
$a127m285$	$\{4,2\}$	0.376(52)		0.1166(54)	0.24(62)	0.629(63)			1.74
$a127m285$	$\{4^{N\pi},2\}$	0.326(20)		0.1114(28)	−0.46(31)	0.708(46)			1.72
$a127m285$	$\{4,3^*\}$	0.376(52)	0.776(59)	0.1176(41)	0.29(60)	0.584(31)	0.048(45)	1.17(78)	1.69
$a127m285$	$\{4^{N\pi},3^*\}$	0.326(20)	0.688(61)	0.1118(28)	−0.59(42)	0.696(68)	−0.12(12)	2.6(1.2)	1.73
$a127m285$	$\{4,2^{\text{free}}\}$	0.359(35)		0.1148(41)	−0.01(59)	0.651(52)			1.81
$a094m270$	$\{4,2\}$	0.273(63)		0.0796(88)	−0.19(52)	0.77(18)			1.22
$a094m270$	$\{4^{N\pi},2\}$	0.2643(95)		0.0784(27)	−0.24(37)	0.80(10)			1.25
$a094m270$	$\{4,3^*\}$	0.273(63)	0.567(83)	0.0855(53)	0.44(49)	0.473(98)	0.28(13)	1.02(89)	1.23
$a094m270$	$\{4^{N\pi},3^*\}$	0.2643(95)	0.56(15)	0.0850(33)	0.40(38)	0.47(13)	0.29(12)	1.00(88)	1.23
$a094m270$	$\{4,2^{\text{free}}\}$	0.485(42)		0.0951(22)	6.8(3.6)	0.586(20)			1.06
$a094m270L$	$\{4,2\}$	0.303(42)		0.0822(35)	0.74(95)	0.680(47)			1.08
$a094m270L$	$\{4^{N\pi},2\}$	0.249(27)		0.0767(36)	−0.18(45)	0.775(75)			1.57
$a094m270L$	$\{4,3^*\}$	0.303(42)	0.561(83)	0.0834(23)	1.29(99)	0.588(53)	0.23(13)	−1.2(3.4)	0.95
$a094m270L$	$\{4^{N\pi},3^*\}$	0.249(27)	0.440(61)	0.0806(21)	0.55(36)	0.534(61)	0.316(93)	−0.001213(3)	0.93
$a094m270L$	$\{4,2^{\text{free}}\}$	0.344(26)		0.0849(16)	2.4(1.6)	0.654(16)			1.02
$a091m170$	$\{4,2\}$	0.293(45)		0.0682(57)	0.89(95)	0.94(14)			0.98
$a091m170$	$\{4^{N\pi},2\}$	0.195(19)		0.0473(71)	−0.92(67)	1.78(43)			1.34
$a091m170$	$\{4,3^*\}$	0.293(45)	0.578(81)	0.0696(39)	1.4(1.2)	0.81(15)	0.28(41)	−1.2(4.9)	1.04
$a091m170$	$\{4^{N\pi},3^*\}$	0.195(19)	0.413(66)	0.0609(59)	0.7(1.7)	0.76(43)	0.59(69)	0.05(4)	1.02
$a091m170$	$\{4,2^{\text{free}}\}$	0.320(51)		0.0702(50)	1.5(1.7)	0.89(11)			1.02
$a091m170L$	$\{4,2\}$	0.252(36)		0.0630(65)	0.73(69)	1.03(20)			1.15
$a091m170L$	$\{4^{N\pi},2\}$	0.157(11)		0.0337(72)	−1.44(99)	2.77(86)			1.63
$a091m170L$	$\{4,3^*\}$	0.252(36)	0.530(38)	0.0647(49)	1.00(66)	0.90(17)	0.16(28)	−0.02(1)	1.23
$a091m170L$	$\{4^{N\pi},3^*\}$	0.157(11)	0.386(73)	0.0596(75)	1.13(59)	0.54(37)	0.89(18)	−0.06(1)	1.27
$a091m170L$	$\{4,2^{\text{free}}\}$	0.297(43)		0.0694(51)	2.1(1.7)	0.87(11)			1.25
$va073m270$	$\{4,2\}$	0.229(41)		0.0612(45)	0.17(77)	0.76(11)			0.98
$a073m270$	$\{4^{N\pi},2\}$	0.217(24)		0.0598(31)	−0.05(47)	0.792(82)			1.02
$a073m270$	$\{4,3^*\}$	0.229(41)	0.386(79)	0.0633(25)	0.97(71)	0.563(64)	0.35(11)	−0.9(1.2)	1.03
$a073m270$	$\{4^{N\pi},3^*\}$	0.217(24)	0.363(79)	0.0626(16)	0.83(44)	0.545(75)	0.383(86)	−0.75(87)	1.03
$a073m270$	$\{4,2^{\text{free}}\}$	0.311(16)		0.0670(10)	3.3(1.3)	0.695(15)			1.56
$a071m170$	$\{4,2\}$	0.216(36)		0.0495(48)	0.8(1.2)	0.95(17)			1.39
$a071m170$	$\{4^{N\pi},2\}$	0.151(12)		0.0402(37)	−0.11(62)	1.26(22)			0.98
$a071m170$	$\{4,3^*\}$	0.216(36)	0.443(40)	0.0537(27)	2.5(1.3)	0.520(92)	0.69(13)	−2.4(3.2)	1.10
$a071m170$	$\{4^{N\pi},3^*\}$	0.151(12)	0.398(31)	0.0495(31)	1.50(55)	0.44(15)	0.91(13)	−0.9(1.3)	1.11
$a071m170$	$\{4,2^{\text{free}}\}$	0.352(56)		0.0586(23)	19(19)	0.771(34)			1.21

Table 7. Comparison of results of the fits to remove the excited-state contamination for the momentum fraction $\langle x \rangle_{u-d}$ using the five strategies, $\{4,2\}$, $\{4^{N\pi},2\}$, $\{4,3^*\}$, $\{4^{N\pi},3^*\}$ and $\{4,2^{\text{free}}\}$. The fit parameters, defined in eq. (5.2), are given for all seven ensembles along with the χ^2/dof of the fit.

JHEP04(2021)044

$\langle x \rangle_{\Delta u - \Delta d}$									
Ensemble	fit-type	$a\Delta M_1$	$a\Delta M_2$	$\langle 0\|\mathcal{O}\|0\rangle$	$\frac{\langle 1\|\mathcal{O}\|1\rangle \|A_1\|^2}{\langle 0\|\mathcal{O}\|0\rangle \|A_0\|^2}$	$\frac{\langle 1\|\mathcal{O}\|0\rangle \|A_1\|}{\langle 0\|\mathcal{O}\|0\rangle \|A_0\|}$	$\frac{\langle 2\|\mathcal{O}\|0\rangle \|A_2\|}{\langle 0\|\mathcal{O}\|0\rangle \|A_0\|}$	$\frac{\langle 2\|\mathcal{O}\|1\rangle \|A_2\|\|A_1\|}{\langle 0\|\mathcal{O}\|0\rangle \|A_0\|^2}$	χ^2/dof
$a127m285$	$\{4,2\}$	0.376(52)		0.1404(38)	−0.19(35)	0.404(30)			1.10
$a127m285$	$\{4^{N\pi},2\}$	0.326(20)		0.1363(24)	−0.25(25)	0.431(30)			1.30
$a127m285$	$\{4,3^*\}$	0.376(52)	0.776(59)	0.1443(24)	0.40(41)	0.252(51)	0.529(94)	−0.6(1.7)	1.07
$a127m285$	$\{4^{N\pi},3^*\}$	0.326(20)	0.688(61)	0.1445(33)	0.59(49)	0.162(96)	0.62(30)	−0.04(2.14)	0.83
$a127m285$	$\{4,2^{\text{free}}\}$	0.706(58)		0.1503(14)	15(12)	0.532(28)			1.20
$a094m270$	$\{4,2\}$	0.273(63)		0.0960(80)	−0.01(41)	0.56(12)			1.30
$a094m270$	$\{4^{N\pi},2\}$	0.2643(95)		0.0949(27)	−0.05(31)	0.574(74)			1.33
$a094m270$	$\{4,3^*\}$	0.273(63)	0.567(83)	0.1048(40)	0.80(43)	0.20(11)	0.69(11)	−0.29(80)	1.09
$a094m270$	$\{4^{N\pi},3^*\}$	0.2643(95)	0.56(15)	0.1048(52)	0.80(48)	0.19(18)	0.703(96)	−0.30(85)	1.09
$a094m270$	$\{4,2^{\text{free}}\}$	0.689(50)		0.1136(18)	39(22)	0.692(28)			0.94
$a094m270L$	$\{4,2\}$	0.303(42)		0.0971(30)	0.19(59)	0.543(25)			1.26
$a094m270L$	$\{4^{N\pi},2\}$	0.249(27)		0.0940(26)	0.18(39)	0.499(39)			1.30
$a094m270L$	$\{4,3^*\}$	0.303(42)	0.561(83)	0.0986(19)	1.14(65)	0.418(63)	0.497(96)	−3.1(3.5)	0.86
$a094m270L$	$\{4^{N\pi},3^*\}$	0.249(27)	0.440(61)	0.0970(17)	0.83(41)	0.324(68)	0.540(87)	−1.4(1.3)	0.85
$a094m270L$	$\{4,2^{\text{free}}\}$	0.400(53)		0.1015(18)	4.4(4.5)	0.559(35)			1.11
$a091m170$	$\{4,2\}$	0.293(45)		0.0794(57)	−0.12(56)	0.83(12)			1.36
$a091m170$	$\{4^{N\pi},2\}$	0.195(19)		0.0646(59)	−0.73(43)	1.14(21)			1.39
$a091m170$	$\{4,3^*\}$	0.293(45)	0.578(81)	0.0848(32)	0.69(78)	0.52(11)	0.48(27)	1.3(3.2)	1.02
$a091m170$	$\{4^{N\pi},3^*\}$	0.195(19)	0.413(66)	0.0802(53)	0.58(71)	0.36(23)	0.65(27)	0.3(1.5)	1.03
$a091m170$	$\{4,2^{\text{free}}\}$	0.441(64)		0.0899(28)	6.6(6.4)	0.72(3)			1.09
$a091m170L$	$\{4,2\}$	0.252(36)		0.0721(69)	−0.25(48)	1.00(19)			0.81
$a091m170L$	$\{4^{N\pi},2\}$	0.157(11)		0.0453(67)	−1.54(68)	2.11(49)			0.89
$a091m170L$	$\{4,3^*\}$	0.252(36)	0.530(38)	0.0789(40)	0.72(92)	0.60(13)	0.52(39)	−0.04(4.2)	0.36
$a091m170L$	$\{4^{N\pi},3^*\}$	0.157(11)	0.386(73)	0.0728(87)	0.71(87)	0.42(36)	0.80(36)	−0.02(1.6)	0.35
$a091m170L$	$\{4,2^{\text{free}}\}$	0.388(52)		0.0865(33)	4.6(3.7)	0.76(3)			0.43
$a073m270$	$\{4,2\}$	0.229(41)		0.0747(33)	−0.13(42)	0.542(50)			1.56
$a073m270$	$\{4^{N\pi},2\}$	0.217(24)		0.0737(23)	−0.23(31)	0.555(47)			1.63
$a073m270$	$\{4,3^*\}$	0.229(41)	0.386(79)	0.0780(13)	0.57(30)	0.30(14)	0.630(96)	0.61(97)	1.12
$a073m270$	$\{4^{N\pi},3^*\}$	0.217(24)	0.363(79)	0.0780(17)	0.59(33)	0.25(14)	0.660(84)	0.39(87)	1.12
$a073m270$	$\{4,2^{\text{free}}\}$	0.457(14)		0.0827(5)	24.0(7.1)	0.758(13)			1.28
$a071m170$	$\{4,2\}$	0.216(36)		0.0591(45)	0.1(1.0)	0.81(12)			1.45
$a071m170$	$\{4^{N\pi},2\}$	0.151(12)		0.0466(41)	−0.89(61)	1.29(21)			1.57
$a071m170$	$\{4,3^*\}$	0.216(36)	0.443(40)	0.0645(23)	2.4(1.1)	0.31(12)	1.04(12)	−2.2(2.9)	1.22
$a071m170$	$\{4^{N\pi},3^*\}$	0.151(12)	0.398(31)	0.0645(35)	1.80(50)	0.07(13)	1.23(11)	−1.2(1.2)	1.27
$a071m170$	$\{4,2^{\text{free}}\}$	0.545(23)		0.0711(10)	376(187)	1.046(28)			1.33

Table 8. Comparison of results of the fits to remove the excited-state contamination for the helicity moment $\langle x \rangle_{\Delta u - \Delta d}$. The rest is the same as in table 7.

JHEP04(2021)044

$\langle x \rangle_{\delta u - \delta d}$									
Ensemble	fit-type	$a\Delta M_1$	$a\Delta M_2$	$\langle 0\|\mathcal{O}\|0\rangle$	$\frac{\langle 1\|\mathcal{O}\|1\rangle \|A_1\|^2}{\langle 0\|\mathcal{O}\|0\rangle \|A_0\|^2}$	$\frac{\langle 1\|\mathcal{O}\|0\rangle \|A_1\|}{\langle 0\|\mathcal{O}\|0\rangle \|A_0\|}$	$\frac{\langle 2\|\mathcal{O}\|0\rangle \|A_2\|}{\langle 0\|\mathcal{O}\|0\rangle \|A_0\|}$	$\frac{\langle 2\|\mathcal{O}\|1\rangle \|A_2\|\|A_1\|}{\langle 0\|\mathcal{O}\|0\rangle \|A_0\|^2}$	χ^2/dof
$a127m285$	$\{4, 2\}$	0.376(52)		0.1406(55)	0.10(57)	0.61(5)			1.28
$a127m285$	$\{4^{N_\pi}, 2\}$	0.326(20)		0.1344(33)	−0.22(32)	0.66(5)			1.59
$a127m285$	$\{4, 3^*\}$	0.376(52)	0.776(59)	0.1448(36)	0.51(57)	0.45(6)	0.36(14)	2.5(2.2)	0.82
$a127m285$	$\{4^{N_\pi}, 3^*\}$	0.326(20)	0.688(61)	0.1466(44)	0.30(89)	0.30(15)	0.42(55)	5.4(4.5)	0.57
$a127m285$	$\{4, 2^{\text{free}}\}$	0.64(11)		0.1539(32)	17(21)	0.68(10)			0.81
$a094m270$	$\{4, 2\}$	0.273(63)		0.096(10)	−0.19(53)	0.74(17)			1.63
$a094m270$	$\{4^{N_\pi}, 2\}$	0.2643(95)		0.0944(32)	−0.24(42)	0.76(10)			1.66
$a094m270$	$\{4, 3^*\}$	0.273(63)	0.567(83)	0.1056(53)	0.54(51)	0.34(13)	0.66(15)	1.1(1.2)	1.08
$a094m270$	$\{4^{N_\pi}, 3^*\}$	0.2643(95)	0.56(15)	0.1054(58)	0.54(51)	0.32(20)	0.67(14)	1.1(1.2)	1.08
$a094m270$	$\{4, 2^{\text{free}}\}$	0.633(45)		0.1166(20)	29(15)	0.80(3)			0.86
$a094m270L$	$\{4, 2\}$	0.303(42)		0.0997(35)	−0.30(54)	0.644(31)			0.80
$a094m270L$	$\{4^{N_\pi}, 2\}$	0.249(27)		0.0943(36)	−0.69(33)	0.700(55)			1.06
$a094m270L$	$\{4, 3^*\}$	0.303(42)	0.561(83)	0.1024(20)	0.39(59)	0.460(77)	0.53(13)	3.3(3.3)	0.62
$a094m270L$	$\{4^{N_\pi}, 3^*\}$	0.249(27)	0.440(61)	0.1009(20)	0.31(42)	0.348(85)	0.59(11)	1.4(1.6)	0.64
$a094m270L$	$\{4^{\text{free}}, 2\}$	0.466(29)		0.1066(12)	12.3(7.0)	0.746(25)			0.82
$a091m170$	$\{4, 2\}$	0.293(45)		0.0780(72)	−0.59(93)	1.05(17)			1.17
$a091m170$	$\{4^{N_\pi}, 2\}$	0.195(19)		0.0517(88)	−1.29(78)	2.07(54)			1.89
$a091m170$	$\{4, 3^*\}$	0.293(45)	0.578(81)	0.0834(47)	−0.20(1.07)	0.80(16)	−0.06(39)	10(6)	0.87
$a091m170$	$\{4^{N_\pi}, 3^*\}$	0.195(19)	0.413(66)	0.0754(77)	−0.83(1.2)	0.76(36)	0.14(47)	4.8(2.8)	0.87
$a091m170$	$\{4, 2^{\text{free}}\}$	0.424(61)		0.0904(39)	8.4(7.0)	0.89(4)			0.95
$a091m170L$	$\{4, 2\}$	0.252(36)		0.0766(70)	0.19(62)	0.97(17)			1.27
$a091m170L$	$\{4^{N_\pi}, 2\}$	0.157(11)		0.0430(80)	−1.65(86)	2.5(7)			1.48
$a091m170L$	$\{4, 3^*\}$	0.252(36)	0.530(38)	0.0855(43)	1.64(87)	0.43(17)	1.00(36)	0.3(3)	1.25
$a091m170L$	$\{4^{N_\pi}, 3^*\}$	0.157(11)	0.386(73)	0.0907(148)	1.91(90)	−0.11(43)	1.29(33)	−0.85(2)	1.22
$a091m170L$	$\{4, 2^{\text{free}}\}$	0.339(114)		0.0872(96)	2.8(5.3)	0.82(8)			1.30
$a073m270$	$\{4, 2\}$	0.229(41)		0.0736(49)	−0.65(46)	0.774(92)			1.01
$a073m270$	$\{4^{N_\pi}, 2\}$	0.217(24)		0.0738(29)	−0.43(38)	0.695(68)			0.73
$a073m270$	$\{4, 3^*\}$	0.229(41)	0.386(79)	0.0786(17)	0.38(36)	0.41(14)	0.66(12)	1.3(1.4)	0.79
$a073m270$	$\{4^{N_\pi}, 3^*\}$	0.217(24)	0.363(79)	0.0785(18)	0.40(37)	0.36(15)	0.70(10)	1.0(1.2)	0.80
$a073m270$	$\{4, 2^{\text{free}}\}$	0.431(16)		0.0843(7)	17.7(5.6)	0.868(14)			1.11
$a071m170$	$\{4, 2\}$	0.216(36)		0.0607(54)	−1.50(98)	0.97(16)			1.23
$a071m170$	$\{4^{N_\pi}, 2\}$	0.151(12)		0.0460(51)	−2.15(72)	1.60(31)			1.28
$a071m170$	$\{4, 3^*\}$	0.216(36)	0.443(40)	0.0673(32)	0.2(1.1)	0.44(13)	0.94(14)	1.4(3.4)	1.10
$a071m170$	$\{4^{N_\pi}, 3^*\}$	0.151(12)	0.398(31)	0.0661(49)	0.62(59)	0.24(17)	1.12(15)	0.4(1.5)	1.15
$a071m170$	$\{4, 2^{\text{free}}\}$	0.498(32)		0.0738(15)	98(81)	1.110(36)			1.19

Table 9. Comparison of results of the fits to remove the excited-state contamination for the transversity moment $\langle x \rangle_{\delta u - \delta d}$. The rest is the same as in table 7.

JHEP04(2021)044

C Renormalization of the operators

In this appendix, we describe two methods of calculating the renormalization factors, $Z_{VD,AD,TD}$, for the three one-derivative operators specified in eqs. (3.5), (3.6) and (3.7). On the lattice, these Z's are first determined nonperturbatively in the RI′−MOM scheme [58, 59] as a function of the lattice scale $p^2 = p^\mu p^\mu$, and then converted to $\overline{\text{MS}}$ scheme using 3-loop perturbative factors calculated in the continuum in ref. [60]. For data at each p, we perform horizontal matching by choosing the $\overline{\text{MS}}$ scale $\mu = |p|$. These numbers are then run in the continuum $\overline{\text{MS}}$ scheme from scale μ to 2 GeV using three-loop anomalous dimensions [60]. The two methods differ in how the dependence of $Z^{\overline{\text{MS}}}(2\text{GeV})$ on p^2a^2, a lattice artifact, is removed. For details of the three operators and their decomposition into irreducible representations, and for alternate methods for the subtraction of discretization effects using perturbation theory, we refer the reader to refs. [31, 32, 59, 61].

The data for the renormalization factors $Z_{VD,AD,TD}$ in the $\overline{\text{MS}}$ scheme at $\mu = 2\,\text{GeV}$ are shown in figure 11 for the seven ensembles as a function of p^2 — the scale of the RI′−MOM scheme on the lattice. For all three operators, the data do not show a window in p^2 where the results are independent of p^2. We analyze the variation with p^2 as being due to a combination of the breaking of full rotational invariance on the lattice and other p^2 dependent artifacts. Many methods have been proposed to control it, see for example refs. [32, 38, 62]. We use the following two:

- In method A, we take an average over the data points in an interval of 2 GeV^2 about $\hat{p}^2 = \Lambda/a$, where the scale $\Lambda = 3\,\text{GeV}$ is chosen to be large enough to avoid nonperturbative effects and at which perturbation theory is expected to be reasonably well behaved. Also, this choice satisfies both $\hat{p}a \to 0$ and $\Lambda/\hat{p} \to 0$ in the continuum limit as desired. The shaded bands in figures 11 show the window over which the data are averaged (also specified in column three of table 10) and the error (half the height of the band). This method was used in our previous work, PNDME 20, presented in ref. [16].

- In method B, we make a fit to the data using the ansatz $Z(p) = Z_0 + a\sum_\mu p_\mu p_\mu + b(\sum_\mu p_\mu p_\mu)^2$ to remove the p^2 dependent artifacts. The fit is made with p^2 starting at the lower edge of the band used in method A, which is given in column three of table 10, and by which a roughly linear in p^2 behavior is manifest. The results are shown next to the y-axis in figure 11 using the star symbol.

These estimates of Z_{VD}, Z_{AD} and Z_{TD} are summarized in table 10. Using these to renormalize the bare moments given in table 6, the results for the two methods are given in tables 11 and 12. Since the discretization errors are expected to be different in the two methods, therefore, we do not average the values of the renormalization constants but perform the full analysis, including the CCFV fits, for the two methods and compare the results after the continuum extrapolation. These final results after CCFV fits to the data in tables 11 and 12 are summarized in table 4 and found to be consistent.

JHEP04(2021)044

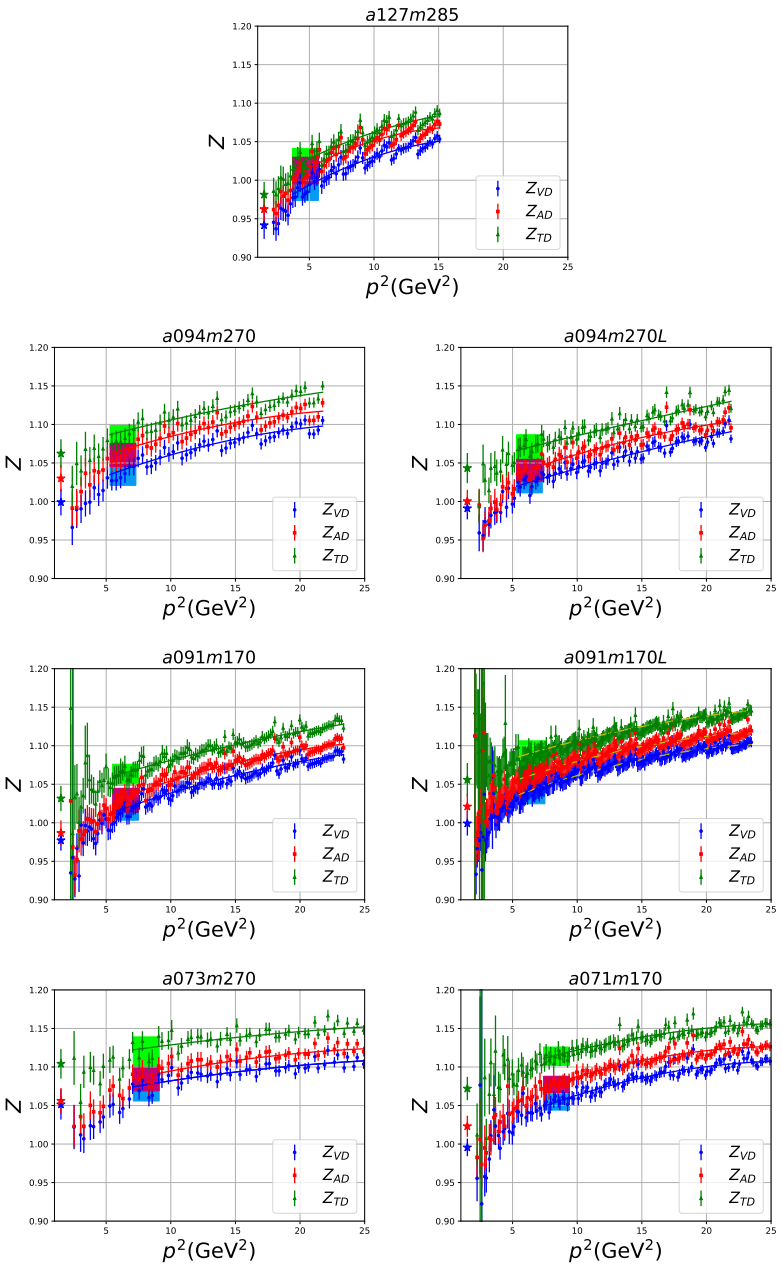

Figure 11. Nonperturbative renormalization factors for $\langle x\rangle_{u-d}$, (Z_{VD}), $\langle x\rangle_{\Delta u-\Delta d}$, (Z_{AD}), and $\langle x\rangle_{\delta u-\delta d}$, (Z_{TD}) in the $\overline{\text{MS}}$ scheme at $\mu = 2$ GeV for the seven ensembles. In all cases, the extent along the x-axis of shaded bands marks the region in p^2 that is averaged in Method A and the height is twice the error in the estimate. The points next to the y-axis with the star symbol give a second estimate (Method B) obtained from a fit with ansatz $Z(p) = Z_0 + ap^2 + bp^4$ to data starting at the left edge of the band.

JHEP04(2021)044

Ensemble	N_{conf}	fit range	Method A			Method B		
		[GeV^2]	Z_{VD}	Z_{AD}	Z_{TD}	Z_{VD}	Z_{AD}	Z_{TD}
$a127m285$	100	3.7–5.7	0.990(16)	1.012(17)	1.026(16)	0.941(14)	0.962(18)	0.981(17)
$a094m270$	100	5.3–7.3	1.036(15)	1.061(15)	1.085(15)	0.999(17)	1.030(18)	1.062(18)
$a094m270L$	100	5.3–7.3	1.025(14)	1.040(14)	1.071(16)	0.991(14)	1.000(15)	1.043(20)
$a091m170$	101	5.5–7.5	1.016(12)	1.029(14)	1.062(14)	0.977(13)	0.987(16)	1.032(16)
$a091m170L$	108	5.5–7.5	1.039(14)	1.058(15)	1.088(18)	0.999(16)	1.021(17)	1.056(22)
$a073m270$	100	7.1–9.1	1.073(17)	1.084(15)	1.120(19)	1.051(20)	1.056(17)	1.104(19)
$a071m170$	112	7.4–9.4	1.054(10)	1.077(11)	1.114(12)	0.996(11)	1.023(14)	1.072(15)

Table 10. Results for the renormalization factors, $Z_{VD,AD,TD}$, in the $\overline{\text{MS}}$ scheme at 2 GeV. These are calculated in the RI'-MOM scheme as a function of scale $p = \sqrt{p_\mu p_\mu}$ on the lattice, matched to the $\overline{\text{MS}}$ scheme at the same scale $\mu = p$, and then run in the continuum $\overline{\text{MS}}$ scheme from μ to 2 GeV. Results are given for two methods used to remove the p^2 dependent artifacts as described in the text. In method A (columns 4–6), the Z's are obtained by averaging the data shown in figure 11 over the range of p^2 specified in the in the third column. Results using method B (columns 7–9) are obtained using fits to the data starting at the lower value of p^2 given in column 3 with the ansatz $Z(p) = Z_0 + ap^2 + bp^4$.

moment	strategy	$a127m285$	$a094m270$	$a094m270L$	$a091m170$	$a091m170L$	$a073m270$	$a071m170$
$\langle x\rangle_{u-d}$	$\{4^{N_\pi}, 3^*\}$	0.179(5)	0.197(8)	0.177(5)	0.150(15)	0.151(18)	0.181(5)	0.160(10)
$\langle x\rangle_{u-d}$	$\{4, 3^*\}$	0.188(7)	0.197(9)	0.183(5)	0.170(9)	0.162(12)	0.183(7)	0.172(8)
$\langle x\rangle_{u-d}$	$\{4, 2^{\text{free}}\}$	0.184(7)	0.211(6)	0.187(4)	0.171(12)	0.174(13)	0.193(4)	0.188(8)
$\langle x\rangle_{\Delta u-\Delta d}$	$\{4^{N_\pi}, 3^*\}$	0.237(7)	0.235(10)	0.217(5)	0.200(13)	0.188(22)	0.228(6)	0.213(11)
$\langle x\rangle_{\Delta u-\Delta d}$	$\{4, 3^*\}$	0.236(5)	0.235(10)	0.220(5)	0.210(8)	0.202(10)	0.227(5)	0.211(7)
$\langle x\rangle_{\Delta u-\Delta d}$	$\{4, 2^{\text{free}}\}$	0.246(5)	0.255(6)	0.226(5)	0.222(8)	0.221(9)	0.241(4)	0.233(4)
$\langle x\rangle_{\delta u-\delta d}$	$\{4^{N_\pi}, 3^*\}$	0.244(8)	0.241(11)	0.232(6)	0.194(20)	0.241(39)	0.237(7)	0.226(17)
$\langle x\rangle_{\delta u-\delta d}$	$\{4, 3^*\}$	0.240(7)	0.242(13)	0.235(5)	0.213(12)	0.225(11)	0.237(6)	0.228(10)
$\langle x\rangle_{\delta u-\delta d}$	$\{4, 2^{\text{free}}\}$	0.256(7)	0.263(8)	0.245(5)	0.231(10)	0.229(25)	0.254(5)	0.250(6)

Table 11. Renormalized moments for all three fit-strategies with Z factors obtained using Method A defined in this appendix C.

moment	strategy	$a127m285$	$a094m270$	$a094m270L$	$a091m170$	$a091m170L$	$a073m270$	$a071m170$
$\langle x\rangle_{u-d}$	$\{4^{N_\pi}, 3^*\}$	0.171(5)	0.190(8)	0.171(5)	0.144(14)	0.146(18)	0.177(6)	0.152(9)
$\langle x\rangle_{u-d}$	$\{4, 3^*\}$	0.179(6)	0.190(9)	0.177(5)	0.163(9)	0.156(11)	0.179(7)	0.163(8)
$\langle x\rangle_{u-d}$	$\{4, 2^{\text{free}}\}$	0.175(7)	0.204(6)	0.180(4)	0.165(12)	0.167(13)	0.189(5)	0.178(7)
$\langle x\rangle_{\Delta u-\Delta d}$	$\{4^{N_\pi}, 3^*\}$	0.225(7)	0.228(10)	0.208(5)	0.192(13)	0.182(21)	0.222(6)	0.203(11)
$\langle x\rangle_{\Delta u-\Delta d}$	$\{4, 3^*\}$	0.225(5)	0.229(10)	0.211(5)	0.201(8)	0.195(10)	0.221(5)	0.201(7)
$\langle x\rangle_{\Delta u-\Delta d}$	$\{4, 2^{\text{free}}\}$	0.234(5)	0.247(7)	0.217(5)	0.213(8)	0.213(9)	0.235(4)	0.221(4)
$\langle x\rangle_{\delta u-\delta d}$	$\{4^{N_\pi}, 3^*\}$	0.233(8)	0.236(11)	0.226(6)	0.189(19)	0.234(38)	0.233(7)	0.218(16)
$\langle x\rangle_{\delta u-\delta d}$	$\{4, 3^*\}$	0.230(7)	0.237(13)	0.229(6)	0.207(11)	0.218(11)	0.233(6)	0.219(10)
$\langle x\rangle_{\delta u-\delta d}$	$\{4, 2^{\text{free}}\}$	0.244(7)	0.258(8)	0.238(5)	0.224(10)	0.222(25)	0.250(5)	0.241(6)

Table 12. Renormalized moments for all three fit-strategies with Z factors obtained using Method B defined in this appendix C.

JHEP04(2021)044

References

[1] STAR collaboration, *Gluon polarization and jet production at STAR*, *Nuovo Cim. C* **036** (2013) 35 [arXiv:1303.0543] [INSPIRE].

[2] PHENIX collaboration, *Inclusive double-helicity asymmetries in neutral-pion and η-meson production in $\vec{p}+\vec{p}$ collisions at $\sqrt{s} = 200$ GeV*, *Phys. Rev. D* **90** (2014) 012007 [arXiv:1402.6296] [INSPIRE].

[3] J. Dudek et al., *Physics Opportunities with the 12 GeV upgrade at Jefferson Lab*, *Eur. Phys. J. A* **48** (2012) 187 [arXiv:1208.1244] [INSPIRE].

[4] A. Accardi et al., *Electron ion collider: the next QCD frontier: understanding the glue that binds us all*, *Eur. Phys. J. A* **52** (2016) 268 [arXiv:1212.1701] [INSPIRE].

[5] CTEQ collaboration, *Handbook of perturbative QCD: version 1.0*, *Rev. Mod. Phys.* **67** (1995) 157 [INSPIRE].

[6] X. Ji, Y.-S. Liu, Y. Liu, J.-H. Zhang and Y. Zhao, *Large-momentum effective theory*, arXiv:2004.03543 [INSPIRE].

[7] B. Yoon et al., *Nucleon transverse momentum-dependent parton distributions in lattice QCD: renormalization patterns and discretization effects*, *Phys. Rev. D* **96** (2017) 094508 [arXiv:1706.03406] [INSPIRE].

[8] M. Diehl, *Generalized parton distributions*, *Phys. Rept.* **388** (2003) 41 [hep-ph/0307382] [INSPIRE].

[9] K. Cichy and M. Constantinou, *A guide to light-cone PDFs from Lattice QCD: an overview of approaches, techniques and results*, *Adv. High Energy Phys.* **2019** (2019) 3036904 [arXiv:1811.07248] [INSPIRE].

[10] N. Karthik, *Lattice computations of PDF: challenges and progress*, talk given at 37th *International Conference on Lattice Field Theory (LATTICE 2019)*, June 16–22, Wuhan, China (2019).

[11] H.-W. Lin et al., *Parton distributions and lattice QCD calculations: a community white paper*, *Prog. Part. Nucl. Phys.* **100** (2018) 107 [arXiv:1711.07916] [INSPIRE].

[12] M. Constantinou et al., *Parton distributions and lattice QCD calculations: toward 3D structure*, arXiv:2006.08636 [INSPIRE].

[13] Flavour Lattice Averaging Group collaboration, *FLAG review 2019: Flavour Lattice Averaging Group (FLAG)*, *Eur. Phys. J. C* **80** (2020) 113 [arXiv:1902.08191] [INSPIRE].

[14] R. Gupta et al., *Isovector charges of the nucleon from 2 + 1 + 1-flavor lattice QCD*, *Phys. Rev. D* **98** (2018) 034503 [arXiv:1806.09006] [INSPIRE].

[15] R. Edwards, *U.S. 2 + 1 flavor clover lattice generation program*, unpublished (2016).

[16] S. Mondal, R. Gupta, S. Park, B. Yoon, T. Bhattacharya and H.-W. Lin, *Moments of nucleon isovector structure functions in 2 + 1 + 1-flavor QCD*, *Phys. Rev. D* **102** (2020) 054512 [arXiv:2005.13779] [INSPIRE].

[17] C. Morningstar and M.J. Peardon, *Analytic smearing of* SU(3) *link variables in lattice QCD*, *Phys. Rev. D* **69** (2004) 054501 [hep-lat/0311018] [INSPIRE].

JHEP04(2021)044

[18] B. Sheikholeslami and R. Wohlert, *Improved continuum limit lattice action for QCD with Wilson fermions*, *Nucl. Phys. B* **259** (1985) 572 [INSPIRE].

[19] M. Lüscher, S. Sint, R. Sommer, P. Weisz and U. Wolff, *Nonperturbative $O(a)$ improvement of lattice QCD*, *Nucl. Phys. B* **491** (1997) 323 [hep-lat/9609035] [INSPIRE].

[20] S. Duane, A.D. Kennedy, B.J. Pendleton and D. Roweth, *Hybrid Monte Carlo*, *Phys. Lett. B* **195** (1987) 216 [INSPIRE].

[21] B. Yoon et al., *Isovector charges of the nucleon from $2+1$-flavor QCD with clover fermions*, *Phys. Rev. D* **95** (2017) 074508 [arXiv:1611.07452] [INSPIRE].

[22] G.S. Bali, S. Collins and A. Schafer, *Effective noise reduction techniques for disconnected loops in Lattice QCD*, *Comput. Phys. Commun.* **181** (2010) 1570 [arXiv:0910.3970] [INSPIRE].

[23] T. Blum, T. Izubuchi and E. Shintani, *New class of variance-reduction techniques using lattice symmetries*, *Phys. Rev. D* **88** (2013) 094503 [arXiv:1208.4349] [INSPIRE].

[24] S. Gusken, K. Schilling, R. Sommer, K.H. Mutter and A. Patel, *Mass splittings in the baryon octet and the nucleon σ term in lattice QCD*, *Phys. Lett. B* **212** (1988) 216 [INSPIRE].

[25] B. Yoon et al., *Controlling excited-state contamination in nucleon matrix elements*, *Phys. Rev. D* **93** (2016) 114506 [arXiv:1602.07737] [INSPIRE].

[26] R. Babich et al., *Adaptive multigrid algorithm for the lattice Wilson-Dirac operator*, *Phys. Rev. Lett.* **105** (2010) 201602 [arXiv:1005.3043] [INSPIRE].

[27] M.A. Clark, R. Babich, K. Barros, R.C. Brower and C. Rebbi, *Solving lattice QCD systems of equations using mixed precision solvers on GPUs*, *Comput. Phys. Commun.* **181** (2010) 1517 [arXiv:0911.3191] [INSPIRE].

[28] M.A. Clark et al., *Accelerating lattice QCD multigrid on GPUs using fine-grained parallelization*, in the proceedings of the *International Conference for High Performance Computing, Networking, Storage and Analysis (SC16)*, November 13–18, Salt Lake City, U.S.A. (2016).

[29] S. Gusken, U. Low, K.H. Mutter, R. Sommer, A. Patel and K. Schilling, *Nonsinglet axial vector couplings of the baryon octet in lattice QCD*, *Phys. Lett. B* **227** (1989) 266 [INSPIRE].

[30] SciDAC, LHPC, UKQCD collaboration, *The Chroma software system for lattice QCD*, *Nucl. Phys. B Proc. Suppl.* **140** (2005) 832 [hep-lat/0409003] [INSPIRE].

[31] M. Gockeler et al., *Polarized and unpolarized nucleon structure functions from lattice QCD*, *Phys. Rev. D* **53** (1996) 2317 [hep-lat/9508004] [INSPIRE].

[32] T. Harris et al., *Nucleon isovector charges and twist-2 matrix elements with $N_f = 2+1$ dynamical Wilson quarks*, *Phys. Rev. D* **100** (2019) 034513 [arXiv:1905.01291] [INSPIRE].

[33] T. Bhattacharya, S.D. Cohen, R. Gupta, A. Joseph, H.-W. Lin and B. Yoon, *Nucleon charges and electromagnetic form factors from $2+1+1$-flavor lattice QCD*, *Phys. Rev. D* **89** (2014) 094502 [arXiv:1306.5435] [INSPIRE].

[34] G.S. Bali et al., *The moment $\langle x \rangle_{u-d}$ of the nucleon from $N_f = 2$ lattice QCD down to nearly physical quark masses*, *Phys. Rev. D* **90** (2014) 074510 [arXiv:1408.6850] [INSPIRE].

[35] G.S. Bali et al., *$\langle x \rangle_{u-d}$ from lattice QCD at nearly physical quark masses*, *Phys. Rev. D* **86** (2012) 054504 [arXiv:1207.1110] [INSPIRE].

[36] Y.-C. Jang, R. Gupta, B. Yoon and T. Bhattacharya, *Axial vector form factors from lattice QCD that satisfy the PCAC relation*, *Phys. Rev. Lett.* **124** (2020) 072002 [arXiv:1905.06470] [INSPIRE].

JHEP04(2021)044

[37] H. Akaike, *A new look at the statistical model identification*, *IEEE Trans. Autom. Contr.* **19** (1974) 716.

[38] C. Alexandrou et al., *Complete flavor decomposition of the spin and momentum fraction of the proton using lattice QCD simulations at physical pion mass*, *Phys. Rev. D* **101** (2020) 094513 [arXiv:2003.08486] [INSPIRE].

[39] C. Alexandrou et al., *Moments of nucleon generalized parton distributions from lattice QCD simulations at physical pion mass*, *Phys. Rev. D* **101** (2020) 034519 [arXiv:1908.10706] [INSPIRE].

[40] Y.B. Yang et al., *Proton mass decomposition from the QCD energy momentum tensor*, *Phys. Rev. Lett.* **121** (2018) 212001 [arXiv:1808.08677] [INSPIRE].

[41] G.S. Bali, S. Collins, M. Göckeler, R. Rödl, A. Schäfer and A. Sternbeck, *Nucleon generalized form factors from two-flavor lattice QCD*, *Phys. Rev. D* **100** (2019) 014507 [arXiv:1812.08256] [INSPIRE].

[42] C. Alexandrou et al., *Nucleon spin and momentum decomposition using lattice QCD simulations*, *Phys. Rev. Lett.* **119** (2017) 142002 [arXiv:1706.02973] [INSPIRE].

[43] A. Abdel-Rehim et al., *Nucleon and pion structure with lattice QCD simulations at physical value of the pion mass*, *Phys. Rev. D* **92** (2015) 114513 [*Erratum ibid.* **93** (2016) 039904] [arXiv:1507.04936] [INSPIRE].

[44] J.R. Green et al., *Nucleon structure from lattice QCD using a nearly physical pion mass*, *Phys. Lett. B* **734** (2014) 290 [arXiv:1209.1687] [INSPIRE].

[45] Y. Aoki et al., *Nucleon isovector structure functions in* $(2+1)$*-flavor QCD with domain wall fermions*, *Phys. Rev. D* **82** (2010) 014501 [arXiv:1003.3387] [INSPIRE].

[46] LHPC collaboration, *Nucleon structure from mixed action calculations using* $2+1$ *flavors of asqtad sea and domain wall valence fermions*, *Phys. Rev. D* **82** (2010) 094502 [arXiv:1001.3620] [INSPIRE].

[47] T.-J. Hou et al., *New CTEQ global analysis of quantum chromodynamics with high-precision data from the LHC*, *Phys. Rev. D* **103** (2021) 014013 [arXiv:1912.10053] [INSPIRE].

[48] J.J. Ethier, N. Sato and W. Melnitchouk, *First simultaneous extraction of spin-dependent parton distributions and fragmentation functions from a global QCD analysis*, *Phys. Rev. Lett.* **119** (2017) 132001 [arXiv:1705.05889] [INSPIRE].

[49] NNPDF collaboration, *Parton distributions from high-precision collider data*, *Eur. Phys. J. C* **77** (2017) 663 [arXiv:1706.00428] [INSPIRE].

[50] S. Alekhin, J. Blümlein, S. Moch and R. Placakyte, *Parton distribution functions,* α_s*, and heavy-quark masses for LHC Run II*, *Phys. Rev. D* **96** (2017) 014011 [arXiv:1701.05838] [INSPIRE].

[51] A. Accardi, L.T. Brady, W. Melnitchouk, J.F. Owens and N. Sato, *Constraints on large-x parton distributions from new weak boson production and deep-inelastic scattering data*, *Phys. Rev. D* **93** (2016) 114017 [arXiv:1602.03154] [INSPIRE].

[52] H1 and ZEUS collaborations, *Combination of measurements of inclusive deep inelastic* $e^{\pm}p$ *scattering cross sections and QCD analysis of HERA data*, *Eur. Phys. J. C* **75** (2015) 580 [arXiv:1506.06042] [INSPIRE].

[53] S. Dulat et al., *New parton distribution functions from a global analysis of quantum chromodynamics*, *Phys. Rev. D* **93** (2016) 033006 [arXiv:1506.07443] [INSPIRE].

JHEP04(2021)044

[54] L.A. Harland-Lang, A.D. Martin, P. Motylinski and R.S. Thorne, *Parton distributions in the LHC era: MMHT 2014 PDFs*, *Eur. Phys. J. C* **75** (2015) 204 [arXiv:1412.3989] [INSPIRE].

[55] NNPDF collaboration, *A first unbiased global determination of polarized PDFs and their uncertainties*, *Nucl. Phys. B* **887** (2014) 276 [arXiv:1406.5539] [INSPIRE].

[56] D. de Florian, R. Sassot, M. Stratmann and W. Vogelsang, *Extraction of spin-dependent parton densities and their uncertainties*, *Phys. Rev. D* **80** (2009) 034030 [arXiv:0904.3821] [INSPIRE].

[57] D. de Florian, R. Sassot, M. Stratmann and W. Vogelsang, *Global analysis of helicity parton densities and their uncertainties*, *Phys. Rev. Lett.* **101** (2008) 072001 [arXiv:0804.0422] [INSPIRE].

[58] M. Gockeler et al., *Perturbative and nonperturbative renormalization in lattice QCD*, *Phys. Rev. D* **82** (2010) 114511 [*Erratum ibid.* **86** (2012) 099903] [arXiv:1003.5756] [INSPIRE].

[59] M. Constantinou et al., *Perturbatively improving regularization-invariant momentum scheme renormalization constants*, *Phys. Rev. D* **87** (2013) 096019 [arXiv:1303.6776] [INSPIRE].

[60] J.A. Gracey, *Three loop anomalous dimension of the second moment of the transversity operator in the MS-bar and RI-prime schemes*, *Nucl. Phys. B* **667** (2003) 242 [hep-ph/0306163] [INSPIRE].

[61] M. Constantinou et al., *Renormalization of local quark-bilinear operators for $N_f = 3$ flavors of stout link nonperturbative clover fermions*, *Phys. Rev. D* **91** (2015) 014502 [arXiv:1408.6047] [INSPIRE].

[62] T. Bhattacharya, V. Cirigliano, S. Cohen, R. Gupta, H.-W. Lin and B. Yoon, *Axial, scalar and tensor charges of the nucleon from $2 + 1 + 1$-flavor lattice QCD*, *Phys. Rev. D* **94** (2016) 054508 [arXiv:1606.07049] [INSPIRE].

JHEP04(2021)044